2009

A Non-planar CMUT Array for Automotive Blind Spot Detection

Syed Abbas
University of Windsor

Recommended Citation

Abbas, Syed, "A Non-planar CMUT Array for Automotive Blind Spot Detection" (2009). *Electronic Theses and Dissertations.* Paper 113.

A Non-planar CMUT Array for Automotive Blind Spot Detection

by

Syed Yasir Abbas

A Thesis
Submitted to the Faculty of Graduate Studies
through Electrical and Computer Engineering
In Partial Fulfillment of the Requirements
for the Degree of Master of Applied Science
at the University of Windsor

Windsor, Ontario, Canada
2009

Author's Declaration of Originality

I hereby certify that I am the sole author of this thesis/major paper and that no part of this thesis/major paper has been published or submitted for publication.

I certify that, to the best of my knowledge, my thesis/major paper does not infringe upon anyone's copyright nor violate any proprietary rights and that any ideas, techniques, quotations, or any other material from the work of other people included in my thesis, published or otherwise, are fully acknowledged in accordance with the standard referencing practices. Furthermore, to the extent that I have included copyrighted material that surpasses the bounds of fair dealing within the meaning of the Canada Copyright Act, I certify that I have obtained a written permission from the copyright owner(s) to include such materials in my major paper and have included copies of such copyright clearances to my appendix.

I declare that this is a true copy of my dissertation, including any final revisions, as approved by my committee and the Graduate Studies Office, and that this dissertation has not been submitted for a higher degree to any other University or Institution.

Abstract

A discretized hyperbolic paraboloid geometry capacitive micromachined ultrasonic transducer (CMUT) array has been designed and fabricated for automotive blind spot monitoring application. The array is designed for a frequency range of 113-167 kHz, beamwidth of 20 ± 5^0 with a maximum sidelobe intensity of -6dB. An SOI based fabrication technology has been used for the 5x5 array with 5 sensing surfaces along each x and y axis and 7 elevation levels. An assembly and packaging technique has been developed to realize the non-planar geometry in a PGA-68 package. Two new analytical models has been developed to more accurately calculate the deflection profile of a thin square membrane and capacitance change due to both external mechanical pressure and the electrostatic pressure due to the bias voltage. The developed models incorporate the effects of bias voltage, external pressure, fringing field capacitance and large deflections. Both the models exhibit excellent accuracy when compared with IntelliSuite™ FEA results.

To my parents with love

Acknowledgment

At the outset I bow before Almighty GOD, Omnipotent and Omnipresent without whose blessing no human being can do anything. I wish to express my gratitude to those who generously helped me to color the mosaic of this project with tiles of their knowledge, expertise and memory.

I feel great pleasure in expressing my gratitude to my mentor Dr. Sazzadur Chowdhury, who kept full faith in me. His encouraging supervision and assistance in tracking down errors and omissions made it possible for me to finish this work in time.

I would like to express my gratitude to Dr. Raafat Mansour, for allowing me to use the wonderful facility at CIRFE, University of Waterloo. I would also like to thank Mr. Bill Jolley and Mr Siamakh Fouladi for there valuable inputs during my stay at Waterloo. To my lab mate and a wonderful senior colleague, Dr. Md. Mosaddequr Rahman, for his valuable inputs and discussions “☺”.

I would like to thank NSERC and Ontario’s Centre of Excellence (OCE) for their financial support and also Canadian Microelectronic Corporation (CMC) and IntelliSuite™ for there technical support.

I would also like to thank my Uncles and Aunts, Prof. Fazal Mehdi, Dr Alvera Mehdi, Dr. Subodh Bhatnagar and Dr. Neerja Bhatnagar, for there immense love and affection. I can’t close before thanking my sisters, the pillar of strength, and I’m here just because of them.

Table of Content

List of Figures

List of Tables

Chapter 1

Introduction

1.1 Goals

Blind spot detection is critical for safe driving of vehicles during lane change maneuvers as the side view and rear view mirrors don't provide complete coverage of blind spots. A number of side impacts and rear-end collisions happen due to a driver’s inability to monitor the blind spots. Some high-end vehicles use vision based sensors like camera or stand alone ultrasonic sensors to monitor blind spots. Due to high cost, low-end vehicles don’t have any blind spot detection system that can tell a driver if the lane change is safe or not. Cost-effective but high performance blind spot detection or monitoring system for automobiles is highly desirable to save lives and property damage.

The performance of current vision based systems for blind spot monitoring such as side view mirror mounted cameras or lasers are compromised in bad weather. Current technology of electromagnetic radars is too expensive and they need a rotating platform to scan the target area. Ultrasonic sensors are good for short range proximity detection. An array of ultrasonic sensors can be used to form a directional acoustical beam focused at the blind spot of a vehicle. These solutions and their variants require significant processing power to be implemented, adding to system cost, complexity and power requirements. The time delay associated with the intensive processing requirements limits the use of such beamformers in applications where real time implementation is crucial [4, 6]. A non-planar array of ultrasonic sensor that can provide an intrinsically frequency independent constant beamwidth beamforming [4, 6, 10], can be used to realize a cost effective blind spot monitoring system. MEMS based array will take much smaller area and the system can be mounted on the side view mirrors.

In this context, the goal of this research work has been defined to design and fabricate a capacitive micromachined ultrasonic transducer (CMUT) array for blind spot detection in automobiles. The microarray is to provide a broadband frequency impendent beamforming capability without any microelectronic signal processing. Complete design specifications of the CMUT array and individual CMUTs will be carried out using lumped element and finite element analysis (FEA) method to meet the requirements for the target application. The device was then fabricated, packaged and tested for experimental verification.

1.2 Background

Beamforming is another name for spatial filtering where an array of sensors together with appropriate signal processing can either direct or block the radiation or the reception of signals in specified directions. Constructive and destructive interference among the signals received by individual array elements are utilized to control the main lobe size and shape while reducing or eliminating side lobes. Both types of interferences are implemented using microelectronics based digital signal processing (DSP) algorithms that introduces appropriate time delays to the signals received by individual sensor elements to add signals

---

coming from a particular direction in phase while cancelling out the signals arriving from undesired directions [1,2].

Achieving frequency-independent constant beamwidth beamforming in the ultrasonic domain is highly desirable in acoustical ranging, directional speech acquisition, automotive proximity detection system, acoustical imaging and many other applications [5]. However, because the beamwidth of a linear or planar array of ultrasonic sensors is inversely proportional to the frequency, implementation of constant beamwidth broadband beamforming capability over a wide frequency range is a major technological challenge [1]–[3]. Additionally, computationally intensive, microelectronics based algorithms of different complexities for beamforming and beamsteering limit the use of such beamformers in applications where real-time information is crucial, for example, blind-spot monitoring of an automobile using an ultrasonic sensor micro array.

1.3 State-of-the-Art

In recent years, significant progress has been made in the design of MEMS based acoustical sensors [13]-[16]. A planar uniformly spaced 3x3 acoustical sensor microarray is presented in [40]. It is targeted towards hearing aid applications for a frequency range of 350 Hz-18.0 KHz. The diaphragm is made up of polysilicon-germanium (Poly-SiGe) and has a side length of 1.2 µm with sensitivity of 10.2 mV/Pa.

Curvilinear MEMS based ultrasonic array, which is also commercially available, is presented in [41]. It works on a center frequency of 4.0 MHz and has 128 elements. The fabrication is carried out on a planar substrate which is later thinned to make it flexible enough to be mounted to a fixed backplate which maintains the radius of curvature of the desired head. It has been experimentally corroborated that the substrate bending doesn’t affect the performance of the transducer array. This high performance device has shown that the technology can deliver excellent results but fabrication challenges abound for these arrays.

Capacitive micromachined ultrasonic transducer based ring array has been presented by [14]. This array is targeted towards medical imaging applications especially related to B-mode operation, e.g. intravascular applications. It works over a wide range of frequency and has 64 elements spread over a radius of 2 mm with each element having a footprint area of 100x100 μm^2 with a membrane thickness of 0.4 µm, metal electrode thickness of 0.3 µm and an air gap thickness of 0.15 µm. The 3-D images obtained experimentally are of sufficient quality for practical applications.

A new methodology for fabrication of CMUTs is presented in [16]. The transducer membrane and cavity are defined on a SOI wafer and on a prime wafer, respectively. Then, using silicon direct bonding in a vacuum environment, two wafers are bonded together forming the transducer. This new technique offers many advantages over conventional surface micromachining. First, forming a vacuum-sealed cavity is relatively easy since the wafer bonding is performed in a vacuum chamber. Second, this process enables more control over the gap height than the surface micro-machining does, making it possible to fabricate very small gaps.

1.4 Limitations of the Current Models

All the above presented state-of-art-work uses some kind of external digital signal processing to obtain the directional sensitivity. Additionally, it appears that integration and packaging of the sensor microarray with additional microelectronic circuitry necessary for frequency independent constant beamwidth beamforming (FICBB) is challenging in terms of extra die space, low-loss interconnection paths and parasitic capacitance. One possible approach to address this issue is to exploit the geometrical properties of a surface that can intrinsically enable a beamforming capability within a desired frequency range without any microelectronic signal processing for beamforming [6, 10].

1.5 Scientific Approach to Solve the Problem

In [10], it has been established that a continuous aperture hyperbolic paraboloid geometry transducer exhibits an intrinsic property of frequency-independent constant beamwidth beamforming. The geometry exploits the time delay in the medium instead of an electronic delay as used in conventional beamformers to realize a beamforming capability. The design was realized in macroscale, and experimental results were presented that verify the associated mathematical model. The basic concept of intrinsic beamforming comes from synthesis method [42].

The current fabrication technology does not support fabrication of a continuous aperture hyperbolic paraboloid geometry CMUT array. However, [4, 6] suggested that planar technology CMUTs can be fabricated or assembled on a microfabricated tiered geometry that can approximate a discretized hyperbolic paraboloid surface. Such an array can provide an intrinsic constant beamwidth beamforming capability that can match very closely with a continuous aperture hyperbolic paraboloid geometry transducer.

1.6 Target Applications

The developed micro array is targeted towards blind spot detection in automobiles and can be even extended for more complex high frequency ultrasonic imaging applications like medical diagnostic applications. A narrow ultrasonic beam from the non-planar capacitive micromachined ultrasonic transducer (CMUT) array detects other vehicles in blind spots in real-time to warn the driver or apply automatic changes to a vehicle's dynamic control system to avoid a collision or minimize collision damage. This will help in reducing the number of accidents and increasing the safety of the driver and passengers. It can also be used for parking assistance by mounting the CMUT array at the rear end of a car as shown in figure 1.1 and 1.2.

The ultrasonic frequencies should be chosen to minimize signal attenuation in the media and maximize the reflection from the target to allow a large signal to noise ratio (SNR) enabling accurate classification. Also this frequency range should not interfere with system operation and should not affect humans or animals likely to come in proximity of the vehicle. Based on these criteria a frequency range of 113-167 kHz was suggested in [12, 13].

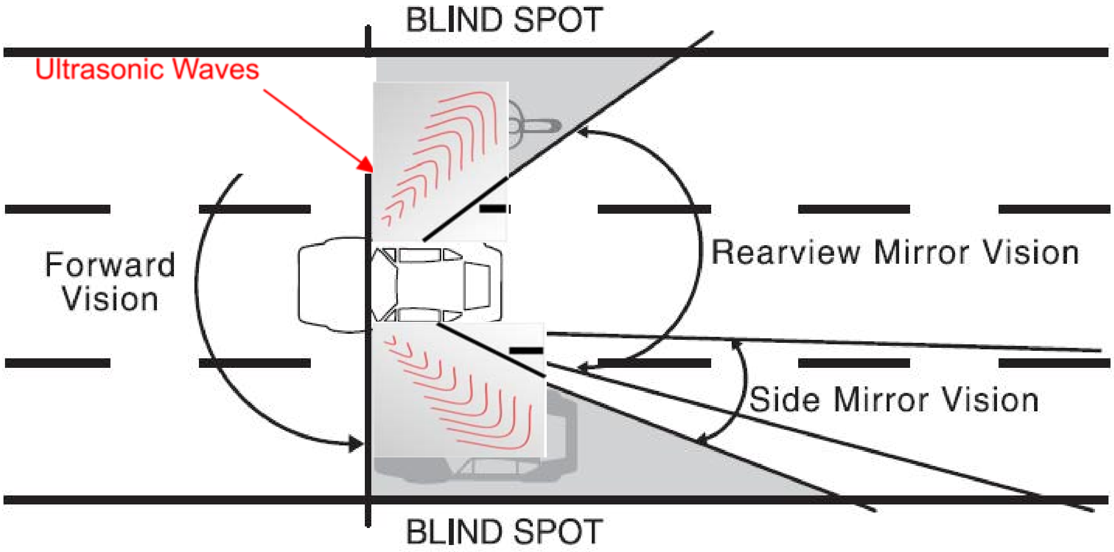

.

Figure 1.1: Blind Spot Detection Scheme.

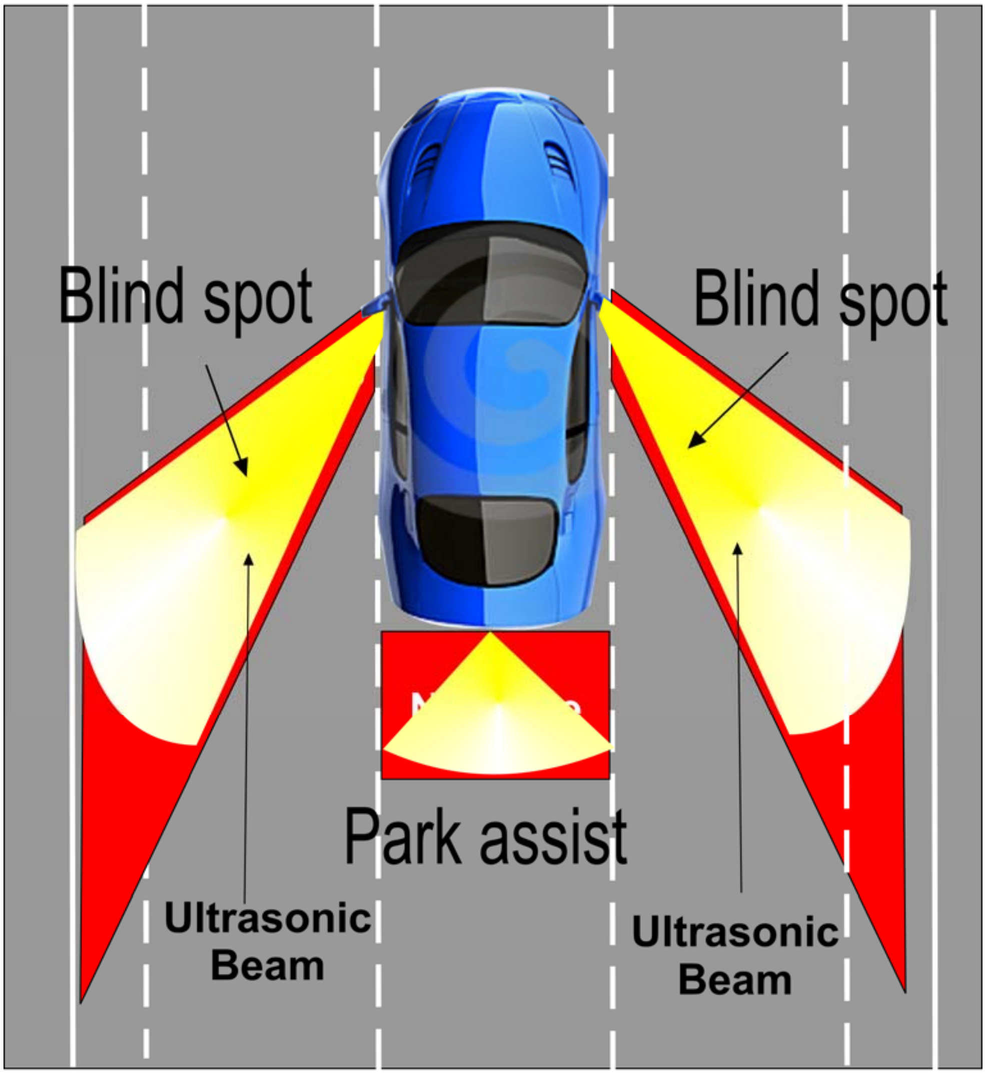

Figure 1.2: Parking Assistance Scheme.

Specific Research Objectives

1 To design a non-planar discretized hyperbolic paraboloid geometry CMUT array for Blind-spot detection in automobiles using the theory developed in [4]. The array is to provide a 20 degrees wide frequency independent intrinsic beamforming capability in the 113-167 kHz frequency range.

2 Develop a highly accurate closed-form analytical model to calculate capacitance change and load deflection profile for CMUTs with square clamped diaphragms, which accounts for the effects of electrostatic pressure due to the bias voltage, fringing field capacitance and large deflections.

3 To carry out analytical and finite element modeling of CMUTs to optimize device geometry while achieving the target performance. This includes the lumped element model used for reduced geometrical complexity and early design parameter optimization.

4 To carry out fabrication simulation to verify the conceptual outputs. Then develop a fabrication process table and necessary mask sets to fabricate the device incorporating the fabrication constraints. Then to carry out the actual fabrication at the Centre for Integrated RF Engineering (CIRFE) at the University of Waterloo, Ontario.

5 Develop the assembling and packaging details for the microarray including the pin-die connection scheme after selection of the appropriate package and have the device assembled and packaged.

1.8 Principle Results

The principle results of this research work have been summarized as follows:-

1. The theory developed by [4] has been used to design capacitive micromachined ultrasonic transducer based non-planar micro array. Two separate design sets have been proposed, both for the frequency range of 113-167 kHz targeted towards blind spot detection in automobiles.
2. Design A is a 7x7 Array having 7 sensing surfaces along each x and y axis, with 13 different elevation levels. The array side length and height is 12.04 mm and 3.18 mm respectively. The beamwidth variation is ±4° with maximum sidelobe intensity of -6dB. Design B is a 5x5 Array having 5 sensing surfaces along each x and y axis, with 7 different elevation levels. The unpackaged array sidelength and height are 9.0 mm and 2.1 mm, respectively. The beamwidth variation is $\pm 5^0$ with maximum sidelobe intensity of -6dB.
3. A new analytical model has been developed to accurately obtain the capacitance change and load deflection profile of a square clamped diaphragm. This model incorporates the effect of biasing voltage, external pressure, fringing field and large deflections.
4. A transducer level design and performance specification for both the designs has been obtained using lumped element model. The 3-D Theromoelectromechanical IntelliSuite™ based FEA has been conducted to verify the results with excellent agreement.

5. The fabrication process has been simulated using IntelliFab module of IntelliSuite™. After simulation, the actual fabrication process incorporating the fabrication constraints has been developed in conjunction with Center of Integrated RF Engineering (CIRFE) of the University of Waterloo. The actual SOI based fabrication of the design B was pursued at CIRFE. Design A was not pursued for fabrication owing to its complex assembling, packaging requirements, and cost involvement.
6. The developed assembly and packaging methodology has been implemented at the AdvoTech Company Inc., Tempe, Arizona, USA to realize the CMUT microarray.

1.9 Organization of Thesis

The Thesis has been organized in the following way:-

In chapter two the array theory developed earlier is used to design the array for the target application. The basic theory behind and the mathematical model for designing discrete hyperbolic paraboloid is presented. The physical parameters of the array have been evaluated using the existing theory. This mathematical model is independent of fabrication technology.

Chapter three deals with the design and simulation of the transducer used, i.e. CMUTs. Since the CMUTs work on the basic principle of capacitance change due to a diaphragm deflection, a novel and easy to implement mathematical model has been developed for rapid determination of the capacitance change and diaphragm deflection profile. This model incorporates the effects of biasing voltage, fringing field capacitance, external pressure, diaphragm geometry and material properties. Lumped element modeling of the CMUTs is also presented in this chapter. The results obtained through the analytical modeling have been cross-verified with results from 3-D electromechanical finite element analysis with excellent accuracy.

Chapter four deals in detail with the fabrication of the CMUTs. The materials used, various fabrication steps and the involved recipes are provided. The conceptual, simulation and actual photographs at various stages have also been provided.

In chapter five assembly and packaging details of the final array has been discussed in detail.

Chapter six makes the concluding remarks, discussions and future scope of in this specific research area.

Chapter 2

Micro-Array Theory

In this chapter detailed design procedure to determine the array level specifications of a discretized hyperbolic paraboloid geometry CMUT array for the target automotive blind spot detection application has been presented. The background of the theory used to develop the array shape and its macro model has been reviewed in detail. Further, the design developed in [6] for MEMS based implementation has been reviewed. Step by step details of the array level design is presented. Once the desired operating frequency range, beamwidth and acceptable beamwidth variation within the operating frequency range are specified, the methodology enables to determine the geometric specification for the array. Transducer level design has been discussed in detail in the next chapter.

2.1 Background

Different approaches to implement constant beamwidth beamforming sensor arrays are available in [1, 5, 8-9]. However, all of them need complex algorithms implemented using a digital signal processing engine to realize a beamforming and beamsteering capability. Although these beamforming techniques produce the desired results to acceptable extent; however, they are complex in nature and the power, cost and time delay associated with the signal processing microelectronics limit the use of such arrays in applications where real time characteristic of the beamforming function is crucial. In [10], it has been established that a frequency independent constant beamwidth beamforming (FICBB) transducer array can be realized by exploiting the surface topology of the array geometry instead of using a microelectronics based digital signal processing beamforming engine. The basic idea behind this line of thought comes from the Synthesis array theory [42].

Following the Synthesis array theory, a reasonably constant beamwidth can be achieved if several basic $Sin(x)/(x)$ beam patterns from a linear array of close proximity transducers can be superimposed in a spatially deflected manner. A graphical representation of the synthesis method [10] has been shown is fig 2.1. Following fig 2.1, several delay lines are used to deflect the basic beam patterns in such a manner that the resulting beamwidth of the array widens at the same rate as the angular beamwidth decreases with frequency. Finally, by using a phase correcting network, the beampatterns are combined in such a way that the phase at the centers of all arrays becomes identical, or in physical terms, the arrays become pivoted about their center.

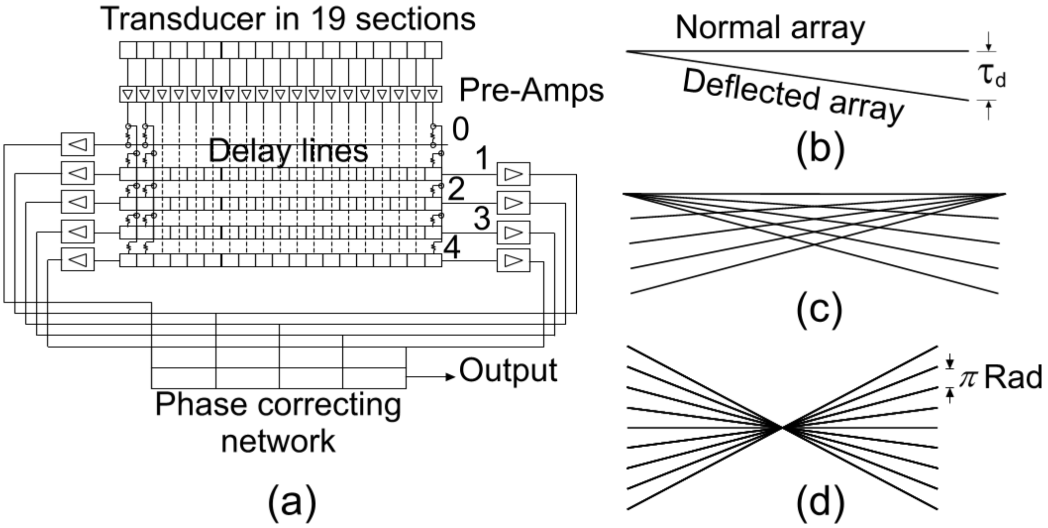

Figure 2.1: Illustration of Synthesis Array Theory and its extension to exploit the delay in the medium to realize a constant beamwidth capability.

A hyperbolic paraboloid surface, as shown in fig 2.2, satisfies the requirement of intrinsic beamforming as suggested by [4, 6, 10]. A square footprint hyperbolic paraboloid surface can be expressed in Cartesian coordinate as:

$$z = y \tan\left(\frac{2\alpha x}{L}\right) \tag{2.1}$$

Where x, y and z are the Cartesian coordinates, L is the sidelength in terms of wavelengths along the x and y directions, respectively and α is the amount of out-of-plane twist in the z direction at the surface extremity measured in degrees from the center of the surface as shown in fig 2.3.

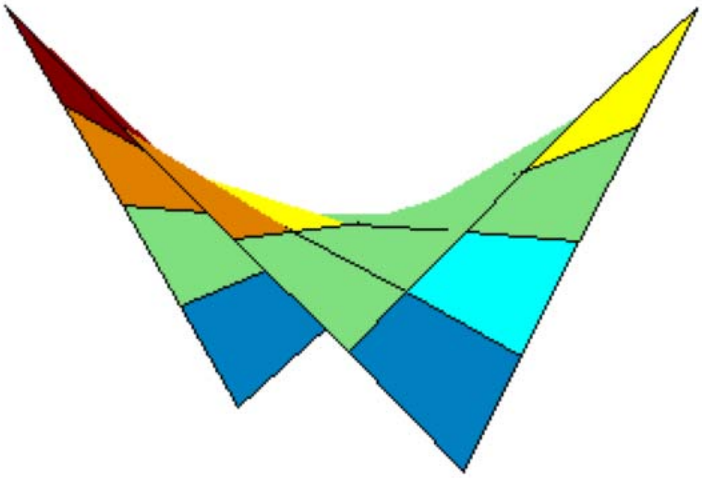

Figure 2.2. A hyperbolic paraboloid surface.

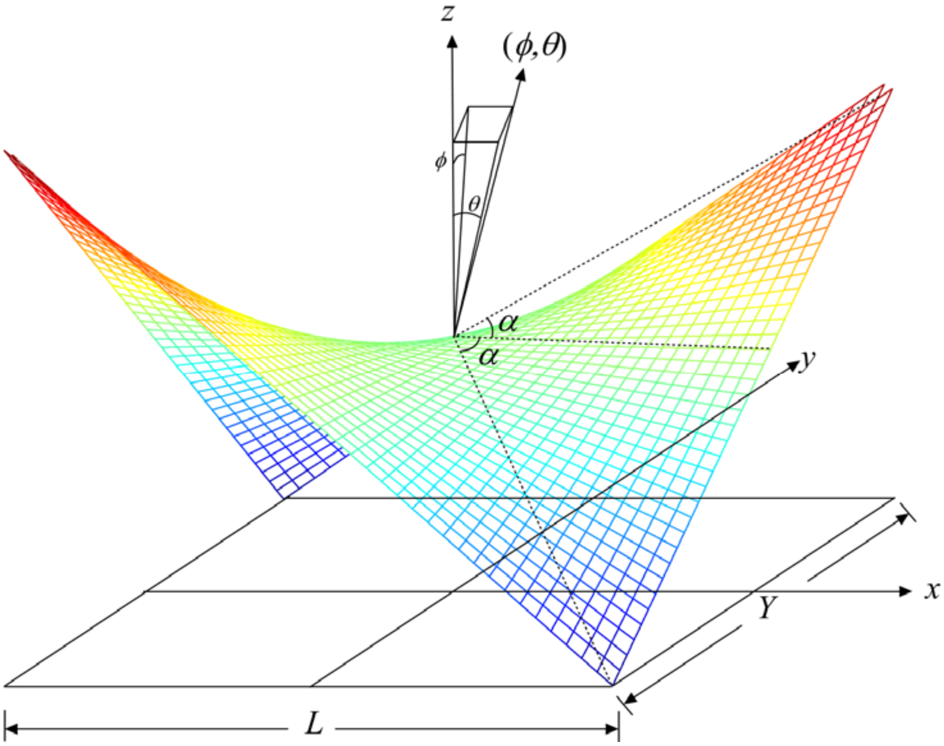

Figure 2.3. Out of plane twist angle α in a Hyperbolic Paraboloid.

Assuming that the out-of-plane angle *α* is small, the generalized array factor $f(\theta,\phi)$ of a continuous aperture hyperbolic paraboloid geometry array in a given direction (θ,ϕ) as referenced from the array normal can be expressed as [10]:

$$f(\theta,\phi) = \frac{1}{LY} \int_{\frac{-L}{2}}^{\frac{L}{2}} \int_{\frac{-Y}{2}}^{\frac{Y}{2}} e^{j2\pi t\left(x\tan\theta + y\tan\phi + \frac{2\alpha xy}{L} \right)} dydx \tag{2.2}$$

where Y and L are the array sidelength along the y and x directions, respectively. The parameter t in (2.2) is defined as:

$$t = \frac{1}{\sqrt{tan^2\theta + tan^2\phi + 1}} \tag{2.3}$$

In [10] it has been shown that the array has a reasonably constant directional response value of $1/(2\alpha L)$ for large values of L with a small out-of-plane twist angle α. However, the array response calculated following (2.2) is valid only if the out of the plane angle α is less than or equal to 10°. For larger values of α, mathematical assumptions made during derivations in [10] lead to considerable error. In [10], (2.2) has been experimentally verified by measuring the array response form a large continuous aperture hyperbolic paraboloid geometry transducer.

Since current microfabrication techniques are basically planar processes that involve successive deposition, patterning, and etching of thin films, a continuous aperture hyperbolic paraboloid geometry transducer array cannot be fabricated using the capabilities of today's microfabrication techniques. As a solution to this problem of fabrication incompatibility, a discretized hyperbolic paraboloid geometry transducer array has been suggested in [4, 6]. This discretized array can provide an intrinsic constant beamwidth beamforming capability that can match very closely with that from a continuous aperture hyperbolic paraboloid geometry transducer. To obtain a discretized version, the

---

double integral in (2.2) has been expressed as the sum of an infinite number of discrete points separated by infinitesimal intervals using standard spatial sampling techniques, such as the Riemann summation [11]. After performing the spatial sampling, the infinite summation can be reduced to a finite one of an arbitrary number of levels. Out of the various Riemann Summation techniques available, center based Riemann Summation was used in this case as it is good for non-monotonic functions and its ability to calculate error bands. Following [14], the center-based Riemann summation in one dimension can be expressed as:

$$\int_a^b f(x) = \lim_{n\to\infty}\sum_{i=1}^{n} f\left(a+\left(i+\frac{1}{2}\right)\frac{b-a}{n}\right)\frac{b-a}{n} \tag{2.4}$$

where n represents the number of discretization levels. The maximum error resulting from this approximation is given as:

$$\left|\int_a^b f(x)dx - A_{mid}\right| \le \frac{M_2(b-a)^3}{12n^2} \tag{2.5}$$

where, M_2 is the maximum value of $|f''(x)|$ and A_{mid} is the value of $f(x)$ at the midpoint of the interval *a-b*.

Applying (2.4) to (2.2) twice, first along x axis and then along y axis, the array factor for the discretized array can be derived as [6]:

$$f(\theta,\phi) = \frac{1}{MN}\sum_{m=0}^{M-1}\sum_{n=0}^{N-1} e^{j2\pi t\left((x')\tan\theta+(y')\tan\phi+\frac{2\alpha x'y'}{L}\right)} \tag{2.6}$$

where:

$$x' = \left(\frac{-L}{2} + \left(m + \frac{1}{2} \right) \frac{L}{M} \right), \quad y' = \left(\frac{-Y}{2} + \left(n + \frac{1}{2} \right) \frac{Y}{N} \right) \qquad (2.7)$$

and M and N are the number of sensing surfaces in the x and y directions respectively.

2.2 Array Geometrical Specification Determination

2.2.1 Array Sidelength

The minimum sidelength *S* of the square footprint discretized hyperbolic paraboloid geometry sensor array can be determined from the following relation [6]:

$$S = \frac{Kc}{f_{lower}} \qquad (2.8)$$

where c is the speed of sound in media and f_{lower} is the lower bound frequency in the operating range. K is the fitting parameter based on the amount of acceptable beam shape variation. As the beamwidth decreases with an increase in the frequency, empirical parameter K maintains the beamwidth within a range of 1-10^0 variations for all the frequencies in a frequency range of $\left(f_{upper} / f_{lower}\right) \leq 40$. Table 2.1 lists some of the values of K for different acceptable beamwidth variation [6].

Table 2.1: Beamwidth Control Parameter *K* Value

K (Unit less)	Beamwidth Variation (°)
3	7
5	5
8	2
10	1

2.1.2 Number of Sensing Surfaces

It has been observed that a linear relationship exists between the number of sensing surfaces and the maximum operating frequency for a pre-specified sidelobe power. Based on numerical simulation results, this relationship has been formulated mathematically using a least-square data-fitting technique to minimize the sidelobe power for all the frequencies in the target range below some pre-specified level while optimizing the number of sensing surfaces *M* and *N* in each direction.

The resulting equations (2.9) and (2.10) specify the number of sensing surfaces per axis for a square footprint array for -10dB and -6dB sidelobe powers, respectively

$$M, N = \left\lceil 5.69 \times \left(\frac{S}{\lambda_{upper}} \right)^{0.5695} - 0.8637 \right\rceil \tag{2.9}$$

$$M, N = \left\lceil 1.49 \times \left(\frac{S}{\lambda_{upper}} \right)^{0.9029} - 0.8484 \right\rceil \tag{2.10}$$

2.1.3 Array Height

The height of the array is directly related to the out of plane twist present at the array extremities. The maximum height measured from the center of a continuous aperture hyperbolic paraboloid geometry array can be determined from the out of plane twist angle α as $S.\tan\alpha$, where S is the sidelength of the array as determined in section 2.2.1. Figure 2.4 shows the relation in a graphical form.

A slight reduction in array height takes place due to the sampling point not occurring at the extremity but at the center of the outermost sensing surface as shown in fig 2.4. However this sampling error introduces an angular error of less than 4.0% for arrays with more than 5 sensing surfaces per axis. This affects the beamwidth by less than 1^{o} [6].

The total height (H) for a discretized square footprint array geometry can be determined using equation (2.11), which has been developed using a curve fitting technique from numerical simulation results obtained using Matlab™ for an out of plane twist angle of 10^{0} [4] .

$$H = \left(-0.5215 \times M^{-0.792} + 0.3762\right)\frac{S.\alpha}{10^{0}} \tag{2.11}$$

where M represents the number of sensing surfaces in each x and y axis.

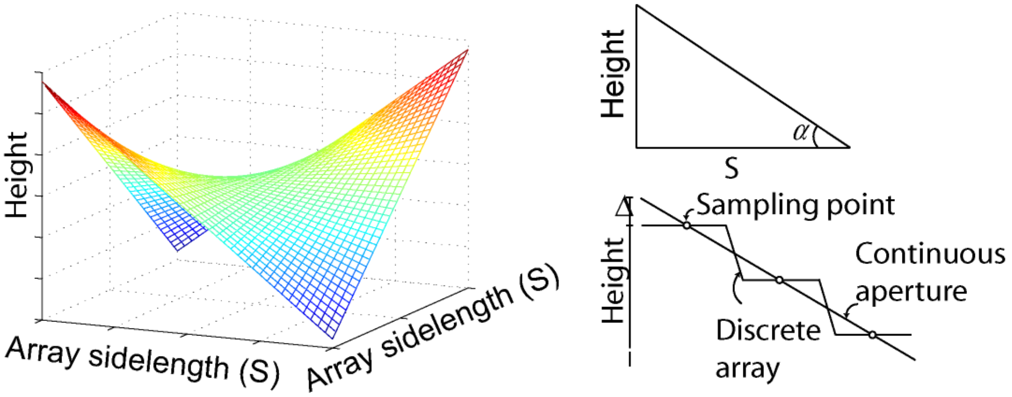

Figure 2.4. Array height sampling

2.3 Array Design for Blind Spot detection

The array geometric design starts with the specifications of the desired operating parameters such as frequency range, beamwidth, and acceptable beamwidth variation. Once the specifications for these parameters are given, the design methodology presented above enables one to determine the necessary geometric specifications for the array in a straightforward manner.

For the target application of Blind spot detection in automobiles the sensor’s operating frequency range should be 113-167 KHz and the maximum sidelobe intensity of less than -6dB [12-13]. Based on these design requirements, two separate designs, design A and design B have been proposed. Table 2.2 lists the determined array geometrical specifications for Design A and a conceptual geometry of design A is shown in figure 2.5. Table 2.3 lists the determined array geometrical specifications for Design B and a conceptual geometry of design B is shown in figure 2.6. The fabrication and assembly constraints have been discussed and incorporated in chapter 4.

Table 2.2. Array Geometrical Specification for Design A

Parameter	**Design A**	**Unit**
Operating Frequency Range	113-167	kHz
Beamwidth Control Parameter (K)	4	--
Beamwidth	20° ± 4°	degrees
Array Sidelength	12.04	mm
Array Height	3.18	mm
Number of elevations	13	
Sensing Surfaces per axis	7	-
Sensing Surface sidelength	1.72	mm

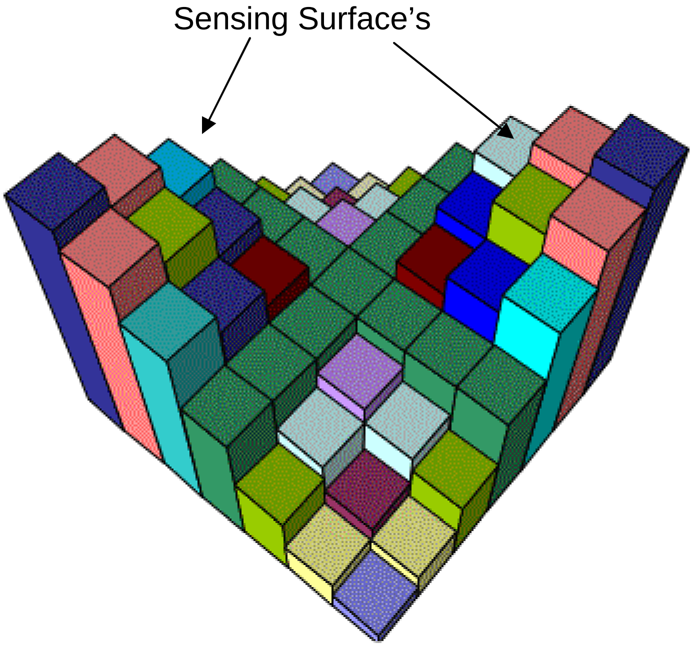

Figure 2.5. Conceptual geometry of Design A (7x7 Array). Sensors having the same elevations have same color.

Table 2.3. Array Geometrical Specifications for Design B

Parameter	**Design B**	**Unit**
Operating Frequency Range	113-167	kHz
Beamwidth Control Parameter (K)	3	--
Beamwidth	20° ± 5°	degrees
Array Sidelength	9.0	mm
Array Height	2.1	mm
Number of elevations	7	
Sensing Surfaces per axis	5	-
Sensing Surface sidelength	1.80	mm

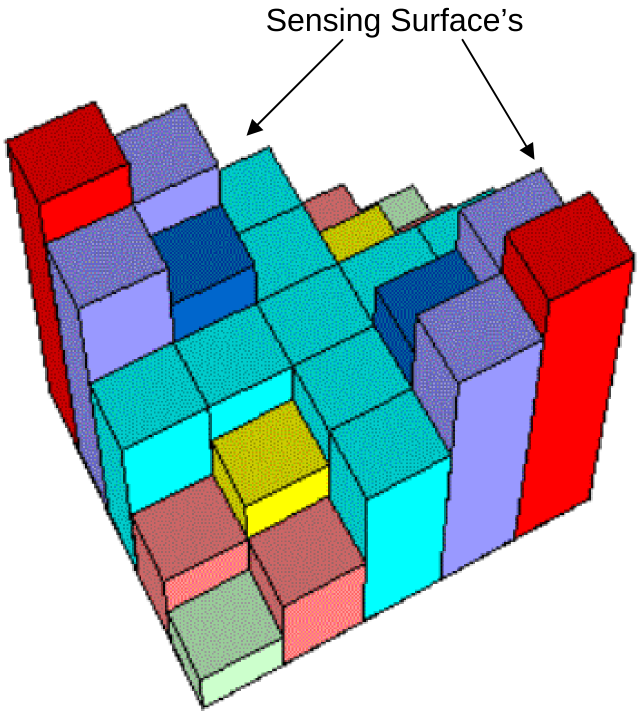

Figure 2.6. Conceptual geometry of Design B (5x5 Array). Sensors having the same elevations have same color.

Chapter 3

CMUT Design and Simulation

This chapter describes the detailed design methodology adopted to design the capacitive micromachined ultrasonic transducers (CMUTs). The mathematical models used to obtain the electrical design, mechanical design and performance parameters have been discussed in detail. A highly accurate analytical model has been developed to calculate capacitance change and deflection profile for MEMS-based capacitive sensors with square membranes. The device performance has been verified using IntelliSuite™.

3.1 Capacitive Micromachined Ultrasonic Transducers (CMUTs): Operating Principle

Capacitive Micromachined Ultrasonic Transducers (CMUTs) are basically capacitive type sensors built with square or circular or hexagonal diaphragm separated from a fixed backplate by a small airgap. Figure 3.1 shows the basic structure of a CMUT with a square membrane. In this case we have used a square shaped membrane owing to its higher fill factor. This type of sensors enjoy the relative advantage of their small size, relatively high sensitivity, batch fabrication capability, inherently low power consumption, low noise features, and ease of IC integration [33-34].

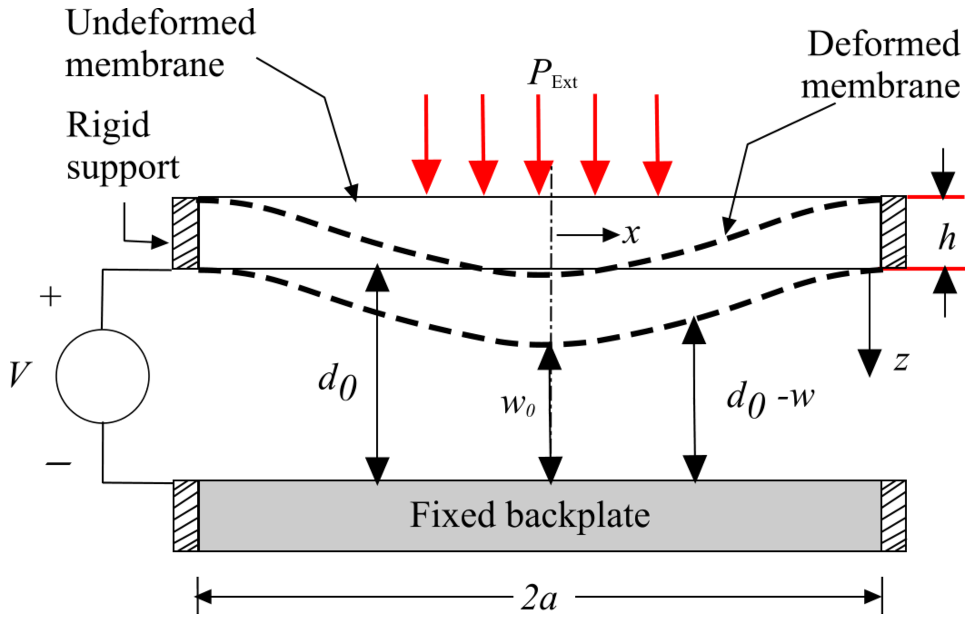

Figure 3.1. Basic Structure of a Capacitive Sensor with a Square Membrane

When exposed to an acoustical sound wave or fluid pressure P_{Ext}, the membrane deflects causing a decrease in the initial airgap d_0 that result in an increase in the capacitance between the membrane and the fixed backplate. To accommodate this increase in capacitance, charges flow from the battery towards the sensor electrodes. When the pressure is withdrawn, the membrane moves back to its undeflected position, the gap increases, and the capacitance decreases. To match this capacitance change, charges flow away from the sensor electrodes towards the battery. In this way, as the membrane vibrates due to an incident acoustical wave or pressure, charges keep flowing to and away from the sensor geometry. When an AC voltage is applied between the electrodes in addition to the bias voltage, a sinusoidal vibration of the membrane is obtained, also known as Transmitting mode. Thus, the same capacitive sensor can be used both as a receiver and as a transmitter.

3.2 New Analytical Model for Capacitance Change

3.2.1 Capacitance Change

The capacitance between a VLSI on-chip interconnect of length L, width W and thickness h separated from an underneath silicon substrate by a dielectric medium of thickness d_0 can be expressed as [35]:

$$C = \varepsilon L\left[\frac{W}{d_0} + 0.77 + 1.06\left(\frac{W}{d_0}\right)^{0.25} + 1.06\left(\frac{h}{d_0}\right)^{0.5}\right] \tag{3.1}$$

where $\varepsilon = \varepsilon_0\varepsilon_r$, ε_0 is the permittivity of free space and ε_r is the relative permittivity of the dielectric layer. The quantity $\varepsilon_0 LW/d_0$ in (3.1) is simply the parallel plate capacitance. The second term within the square bracket is a length (L) dependent adjustment parameter. The third term represents the fringing field capacitance due to the interconnect width (W) while the fourth term represents the fringing field capacitance due to the interconnect thickness (h). Equation (3.1) can be rewritten to express the fringing field capacitances as a function of the parallel plate capacitance in the form:

$$C = C_0 (1 + C_{\text{ff}}) \tag{3.2}$$

where C_0 is the parallel plate capacitance ($\varepsilon_0 LW/d_0$) and C_{ff} is the fringing field factor expressed as:

$$C_{\text{ff}} = 0.77\frac{d_o}{W} + 1.06\left(\frac{d_o}{W}\right)^{0.75} + 1.06\frac{(hd_0)^{0.5}}{W} \tag{3.3}$$

Equations (3.1)-(3.3) can be used to calculate the capacitance between the thin square membrane and the fixed backplate of a CMUT as shown in fig. 1.1. As the membrane is rigidly clamped at the edges and is supported by a dielectric spacer, third term in (3.3) representing the fringing field factor due to the membrane thickness can be neglected as the flux lines originating from the membrane sides don't have any path to terminate on the backplate. Thus, for a square membrane with sidelength $W = L = 2a$, the capacitance between the undeflected membrane and the backplate can be expressed as:

$$C = C_0(1 + C_{\mathrm{ff}}) = \frac{\varepsilon_0 4a^2}{d_0}\left[1 + 0.77\left(\frac{d_0}{2a}\right) + 1.06\left(\frac{d_0}{2a}\right)^{0.75}\right] \tag{3.4}$$

As in the undeformed case, the total capacitance of a deformed membrane under external pressure is also contributed by two factors: the parallel plate capacitance C_{Deform} between the deformed diaphragm and the backplate, and the fringing field capacitance $C_{\mathrm{Deform}} C_{\mathrm{ff}}$ which can be expressed as:

$$C = C_{\mathrm{Deform}}(1 + C_{\mathrm{ff}}) \tag{3.5}$$

Since the edges of the membrane are rigidly fixed and don't undergo any deformation, and as the fringing field is contributed mainly by the charges concentrated at the edges, the fringing field factor C_{ff} can be assumed to remain unchanged due to the deformation of the membrane and C_{ff} can be calculated using (3.3) as before.

Assuming that the diaphragms lies in the $x- y$ plane, the parallel plate capacitance between the deformed membrane and the backplate can be calculated following [36] as:

$$C_{\text{Deform}} = \varepsilon_o \iint_A \frac{dxdy}{d_o - w(x, y)} \tag{3.6}$$

where $w(x, y)$ is vertical displacement of any point on the membrane located at (x, y) and can be determined from the center deflection w_0 using the following relation originally proposed in [37]:

$$w(x, y) = w_0 \, cos\left(\frac{\pi x}{2a}\right) cos\left(\frac{\pi y}{2a}\right) \tag{3.7}$$

The above deflection shape function satisfies the boundary condition of zero bending at the edges. It was observed in [38] that the cosine-like bending shape as expressed in (3.7) does not describe the membrane's actual bending shape accurately. In order to better describe the bending shape of a thin membrane, (3.7) was modified in [38] by adding two more terms as:

$$w(x, y) = \left[w_o + w_1\left(\frac{x^2 + y^2}{a^2}\right) + w_2\left(\frac{x^2 y^2}{a^4}\right)\right] \cos\left(\frac{\pi x}{2a}\right) \cos\left(\frac{\pi y}{2a}\right) \tag{3.8}$$

---

where w_1 and w_2 are two arbitrary parameters expressed as multiples of w_0. Using the energy minimization method, authors in [38] numerically determined parameters w_1 and w_2 as:

$$\left.\begin{aligned} w_1 &= 0.4 w_0 \\ w_2 &= 1.16 w_0 \end{aligned}\right\} \tag{3.9}$$

Though the deflection shape function (3.8) shows excellent agreement with experimental results for deflection profiles of thin diaphragms, investigation shows it does not agree well with the deflection shapes of thick diaphragms that behave more like plates. Further, (3.8) starts deviating for thinner diaphragms with side length less than 1 mm. Authors in [36, 39] used the following deflection shape function for clamped square diaphragm:

$$w(x,y) = w_0 \cos^2\left(\frac{\pi x}{2a}\right)\cos^2\left(\frac{\pi y}{2a}\right) \tag{3.10}$$

This shape function also satisfies the two necessary boundary conditions for a clamped square diaphragm, namely the zero deflection and zero gradients in the deflection profile at diaphragm edge, expressed as [39]:

$$\left.\begin{aligned} &w = 0 \text{ and } \frac{dw}{dx} = 0 \text{ at } x = \pm a \\ &w = 0 \text{ and } \frac{dw}{dy} = 0 \text{ at } y = \pm a \end{aligned}\right\} \tag{3.11}$$

Further investigations reveal that the deflection shape function presented in [38] can predict deflection profiles for thin membranes with a better accuracy than the deflection shape function presented in [39] when compared to FEA results. However, though (3.10) is a poor match for thin membrane deflection profiles, it satisfies the necessary boundary conditions for a clamped square membrane [36, 39]. Therefore, following the approach adopted by the authors in [38], we attempt to extend the deflection shape function in [39] with three more terms with coefficients w_1, w_2 and w_3. The resulting deflection shape function is as follows:

$$w(x,y)=\left[w_0+w_1\left(\frac{x^2+y^2}{a^2}\right)+w_2\left(\frac{x^2y^2}{a^4}\right)+w_3\left(\frac{x^4+y^4}{a^4}\right)\right]\cos^2\left(\frac{\pi x}{2a}\right)\cos^2\left(\frac{\pi y}{2a}\right) \quad (3.12)$$

where the coefficients w_1, w_2, and w_3 can be determined for any specific design space by comparing with the deflection profiles obtained experimentally or from FEA analysis. For the typical design space for MEMS based capacitive type sensors characterized by a square membrane thickness range of 1-3 μm and a membrane sidelength range of 200-1000 μm, the parameters w_1, w_2, and w_3 have been determined by comparing the results from (3.12) with 3-D FEA using IntelliSuite™ for a wide range of device specifications and loading conditions as:

$$\left.\begin{aligned} w_1&=\frac{0.0013}{\sqrt{h}}w_0\\ w_2&=\frac{0.005}{\sqrt{h}}w_0\\ w_3&=\frac{0.0021}{\sqrt{h}}w_0 \end{aligned}\right\} \quad (3.13)$$

---

where h represents the membrane thickness.

The adjustable empirical parameters w_1, w_2, and w_3 in (3.12) will contribute to achieve higher accuracy and make it more suitable to fit deflection profiles for any specific design space.

3.2.2 Electrostatic Pressure

As the DC bias voltage provides a means to realize a voltage signal having the same dynamic characteristics as the incident acoustical or mechanical pressure, the electrostatic attraction force associated with this bias voltage also causes a deflection of the diaphragm. Thus at any time, the total deflection of the diaphragm is the summation of the diaphragm deflection due to external pressure and the diaphragm deflection due to the electrostatic pressure. Thus, the change in capacitance is also a function of diaphragm deflection due to the electrostatic pressure.

Further, this electrostatic attraction force is nonlinear and increases with the decreasing gap between the electrodes for a fixed voltage. When in equilibrium, the total force acting on the diaphragm which is the sum of the electrostatic and the external mechanical pressure will be equal to the elastic restoring force developed in the diaphragm due to its deformation. Hence the effect of Electrostatic force can’t be neglected while calculating the center deflection and hence the capacitance change.

A number of closed-form solutions are available to calculate the deflection of a square diaphragm under large deflection [38]. A simple analytical approach to determine diaphragm deflection and capacitance change as a function of applied pressure for square clamped diaphragms is available in [36, 39]. However, contribution of the bias voltage to the total deflection and thereby the associated change in capacitance has not been considered in the previous works. Moreover, in the previous works, a parallel plate approximation has been used to calculate the capacitance before and after deformation. However, investigation shows that fringing field capacitance associated with the diaphragm edges also contribute to the total capacitance change during the deformation.

The developed electrostatic force after applying a bias voltage V can be derived from the relation:

$$F = -\frac{d}{dx}\left(\frac{1}{2}CV^2\right) = \varepsilon_0 a V^2 \left[\frac{2a}{(d_o - w)^2} + 0.265\frac{(2a)^{0.25}}{(d_o - w)^{1.25}}\right] \tag{3.14}$$

Expanding the terms in the bracket in (3.14) using the Taylor series expansion method about the zero deflection point of the diaphragm center ($w = 0$), neglecting the higher order terms, and after rearrangement one obtains:

$$F = \varepsilon_0 V^2 \left(\frac{4a^2}{d_o^2} + 0.265\frac{(2a)^{0.25}}{d_o^{1.25}}\right) + \varepsilon_0 V^2 \left(\frac{8a^2}{d_o^3} + 0.33125\frac{(2a)^{0.25}}{d_o^{2.25}}\right) w \tag{3.15}$$

Thus the associated electrostatic pressure P_E can be calculated from (3.15) as:

$$P_E = \frac{F}{A} = \frac{\varepsilon_0 V^2}{2a}\left(\frac{2a}{d_o^2} + 0.265\frac{(2a)^{0.25}}{d_o^{1.25}}\right) + \frac{\varepsilon_0 V^2}{2a}\left(\frac{4a}{d_o^3} + 0.33125\frac{(2a)^{0.25}}{d_o^{2.25}}\right) w \tag{3.16}$$

where *A* is the area of the diaphragm. However, as the actual diaphragm motion isn't piston like and the deformation profile of the diaphragm takes a cosine shape, maximum deflection w_0 occurs at the center of the diaphragm. Thus, replacing w by w_0 in (3.16) one obtains the load deflection model of a square diaphragm subject to a linearized electrostatic pressure due to an applied bias voltage V .

3.2.3 Center Deflection

The load-deflection model of a rigidly clamped square diaphragm under large deflection due to an applied uniform pressure P_{Ext} can be expressed as [19]:

$$P_{ext} = C_r \frac{\sigma h}{a^2} w_o + C_b \frac{12D}{a^4} w_o + C_s f_s(v) \frac{\tilde{E} h}{a^4} w_o^3 \tag{3.17}$$

where w_0 is the center deflection, $2a$ is the diaphragm sidelength and h represents the thickness of the diaphragm. In (3.17) $\tilde{E}$ and v represent the effective Young's modulus and the Poisson ratio of the diaphragm material, respectively. *C_r*, *C_b* and *C_s* are constants and are equal to 3.45, 4.06 and 1.994, respectively and $f_s(v)$, a function of v , is given by [38]:

$$f_s(v) = \frac{1-0.271v}{1-v} \tag{3.18}$$

In (3.17) *D* represents the flexural rigidity of the diaphragm and is expressed as:

$$D = \frac{\tilde{E}h^3}{12(1-v^2)} \tag{3.19}$$

whereas the effective Young's modulus $\tilde{E}$ is expressed as:

$$\tilde{E} = \frac{E}{1-\nu^2} \tag{3.20}$$

where E represents the original Young's modulus of the diaphragm material. In equation (3.17), the first term on the right-hand side represents the deflection of the diaphragm due to the residual stress; second term is the deflection due to bending and the third term represent the deflection due to nonlinear spring hardening.

3.2.4 Combined Load Deflection Model

A combined load deflection model of the square diaphragm under electrostatic and external mechanical pressure thus can be obtained by combining (3.16) and (3.17). After combination and rearrangement, one obtains :

$$C_s f_s(v)\frac{Eh}{a^4}w_o^3 + \left[\begin{array}{l} C_r\frac{\sigma h}{a^2} + C_b\frac{12D}{a^4} \\ -\frac{1}{2a}\varepsilon_0 V^2\left(\frac{2a}{d_o^3} + 0.33125\frac{a^{0.25}}{d_o^{2.25}}\right)\end{array}\right]w_o$$

$$-\left[P_M + \frac{1}{2a}\varepsilon_0 V^2\left(\frac{a}{d_o^2} + 0.265\frac{a^{0.25}}{d_o^{1.25}}\right)\right] = 0\,. \tag{3.21}$$

Real root of the above third-order polynomial represents the center deflection w_o of the diaphragm subject to both electrostatic and external pressure. Two other roots are imaginary and have no practical significance. Once the center deflection is known, over-all deflection profile of the diaphragm can be obtained using (3.12) and also the capacitance change using (3.6). This methodology has also been used to obtain the pull-in voltage and the results have been verified by FEA simulations.

3.3 CMUT Lumped Element Model

After determination of the array geometric specifications (Chapter two), transducer level modeling is done to obtain the geometry of individual capacitive sensors and optimize the performance of the sensor. Lumped element modeling is used to reduce the geometric complexity to a manageable level for rapid simulation and specification determination. The lumped element modelling is able to optimize the performance of the individual transducers. This includes modeling of all major sensor performance criteria such as, pull-in voltage, resonant frequency, damping effects and load deflection characteristics [21, 23, 24].

The sensitivity of the CMUT depends mainly on the size and stress of the diaphragm, thickness of the airgap, and the bias voltage.

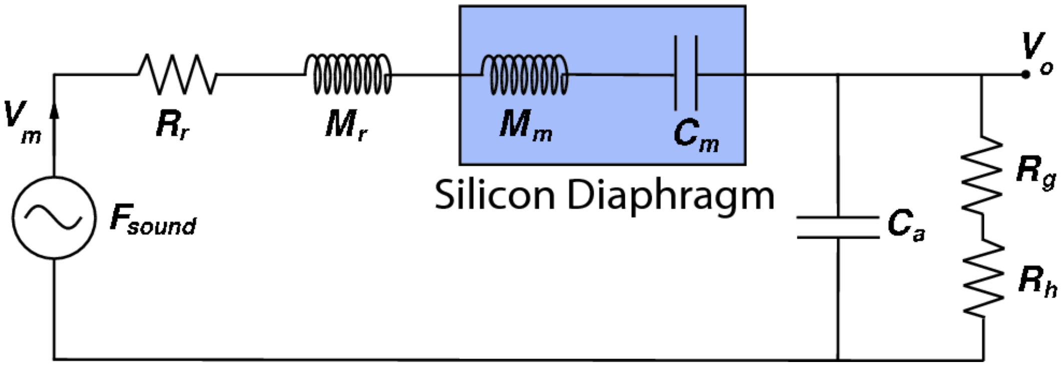

Figure 3.2. Electrical Equivalent Circuit Model of a Capacitive Type Acoustical Sensor

---

The sensitivity and the frequency response of the CMUT can be calculated using an equivalent analog electrical network model of the CMUT [21] as shown in figure 3.2.

In Fig. 3.2, the acoustical force F_{sound} is modeled as an equivalent voltage source and the radiative resistance is R_r. The air mass in contact with the diaphragm subject to displacement is represented by M_r. Theses parameters are defined as [21]:

$$R_r = \frac{\rho_0 a^4 \omega^4}{2\pi c} \tag{3.22}$$

$$M_r = \frac{8\rho_0 a^3}{3\pi\sqrt{\pi}} \tag{3.23}$$

Where ρ_0 is the air density, a is the diaphragm sidelength, ω is the angular vibration frequency $2\pi fc$ and c is the velocity of sound in the media at frequency ω. The mechanical mass of the diaphragm M_m and the diaphragm compliance C_m which is the inverse of the diaphragm stiffness (spring constant) are expressed as.

$$C_m = \frac{32a^2}{\pi^6\left(2\pi^2 D + a^2 T\right)} \tag{3.24}$$

$$M_m = \frac{\pi^4 \rho\left(2\pi^2 D + a^2 T\right)}{64T} \tag{3.25}$$

Where D is the flexural rigidity, and T is the tensile force per unit length.

Viscous losses in the air gap R_g and in the vent hole R_h, and the gap compliance C_a, are given as:

$$R_g = \frac{12\eta a^2}{nd^3\pi}\left(\frac{\alpha}{2} - \frac{\alpha^2}{8} - \frac{\ln(\alpha)}{4} - \frac{3}{8}\right) \tag{3.26}$$

$$R_h \approx \frac{8\eta h a^2}{\pi n r^4} \tag{3.27}$$

$$C_a = \frac{d}{\rho_0 c^2 \alpha^2 a^2} \tag{3.28}$$

Where n is the hole density in the backplate, α is the surface fraction occupied by holes, η is the air viscosity coefficient, d is the average thickness of the airgap, h is the vent height and r is the effective radius of the vent holes. From these definitions we can express the equivalent impedance Z_t of the CMUT as:

$$Z_t = R_r + j\omega(M_r + M_m) + \frac{1}{j\omega C} + \frac{R_g + R_h}{1 + j\omega(R_g + R_h)C_a} \tag{3.29}$$

The total sensitivity S_t of the CMUT is defined as the output voltage V_o per unit of incident acoustical pressure P and can be expressed as [21]:

$$S_t = \frac{V_0}{P} = \frac{V_b a^2}{j\omega d Z_t} \tag{3.30}$$

where V_b is the bias voltage.

The sensitivity presented above lumps the electrical and mechanical components of the system together. This illustrates how the sensitivity scales linearly with bias voltage, but doesn't clearly show the mechanical sensitivity. By separating the sensitivity model between the mechanical and electrical components of the transducer, each component can be evaluated and optimized independently [23]. The mechanical sensitivity can be given in μm/μN as:

$$S_z = \frac{1}{\frac{1}{C_a} + \frac{1}{C_m}} \tag{3.31}$$

3.4 Design Performance and Verification

The theory discussed in the previous sections has been implemented using Matlab™. The result for both the designs A and B have been presented in this section. The IntelliSuite™ 3D electromechanical Analysis has been carried out wherever appropriate. All the Matlab™ codes have been provided in Appendix A. However it has to be noted that only design B (5x5 Array) has been persuaded for fabrication owing to its less complex alignment and packaging requirements. Table 3.1 and 3.2 provides the transducer design specifications and performance specifications for design A (7x7 Array), respectively. Table 3.3 and 3.4 provides the transducer design specifications and performance specifications for design B (5x5 Array), respectively.

The new analytical model developed for capacitance change calculation and deflection profile calculation has been verified using 3D Theromoelectromechanical module of IntelliSuite™. Figure 3.3 shows the relation between the center deflection and applied voltage whereas figure 3.4

---

shows the relation between capacitance and applied voltage. Both the results have been verified by FEA simulation and are in excellent agreement with the model developed. Figure 3.5 shows the relation between center deflection and pressure at 18 volts biasing voltage. These results show that the effect of applied voltage can’t be neglected while calculating either capacitance change or deflection profile.

The sudden jump in the capacitance value seen in the range of 50-60 volts in figure 3.3 is due to pull-in. The pull-in voltage value obtained through the mathematical model is 51.7 Volts where as through FEA (3D Theromoelectromechanical Analysis Module of IntelliSuite$^{\text{TM}}$) is 51.2 Volts. The two values are in excellent agreement with an error of less than 1%. Figure 3.6 shows the displacement versus voltage curve obtained through IntelliSuite™. Figure 3.7 shows the IntelliSuite generated Image of the diaphragm at pull-in. It has to be noted that only a quarter of the diaphragm is used for simulation owing to symmetrical shape and henceforth reducing the processing time.

Table 3.1. Transducer Design Specifications (7x7Array)

Specifications	Value	Unit
Diaphragm per Tier	64	-
Diaphragm Thickness	2.0	µm
Diaphragm Air Gap	1.0	µm
Diaphragm Side length	215	µm
Number of vent holes	4x4	-
Vent Hole dimension	15x15	µm

Table 3.2. Transducer Performance Specifications (7x7Array)

Parameter	Value	Unit
Pull in Voltage	63.53	Volts
Unbiased Tier Capacitance	26.2	pF
Resonant Frequency	512.9	kHz
Diaphragm Area occupied by vent	7.8	%
Mechanical Sensitivity @140kHz	296.7	µm /N
Tier Sensitivity @140kHz	12.24	mV/Pa
Total Array Sensitivity @140kHz	599.8	mV/Pa

Table 3.3. Transducer Design Specifications (5x5Array)

Specifications	Value	Unit
Diaphragm per Tier	6x6	-
Diaphragm Thickness	2.0	µm
Diaphragm Air Gap	1.0	µm
Diaphragm Side length	225	µm
Number of vent holes	5x5	-
Vent Hole dimension	15x15	µm
Inter Dia. Spacing	20	µm
Bonding Space (edges)	175	µm

Table 3.4. Transducer Performance Specifications (5x5Array)

Parameter	Value	Unit
Pull in Voltage	51.72	Volts
Unbiased Tier Capacitance	16.12	pF
Resonant Frequency	480.19	kHz
Diaphragm Area occupied by vent	11.11	%
Mechanical Sensitivity @140kHz	301.61	µm /N
Tier Sensitivity @140kHz	14.24	mV/Pa
Total Array Sensitivity @140kHz	356.0	mV/Pa

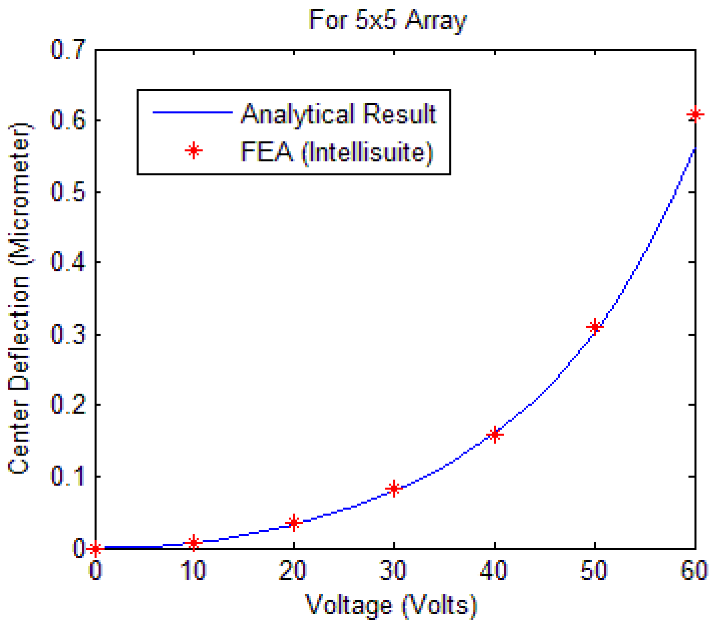

Figure 3.3. Center Deflection Vs Voltage

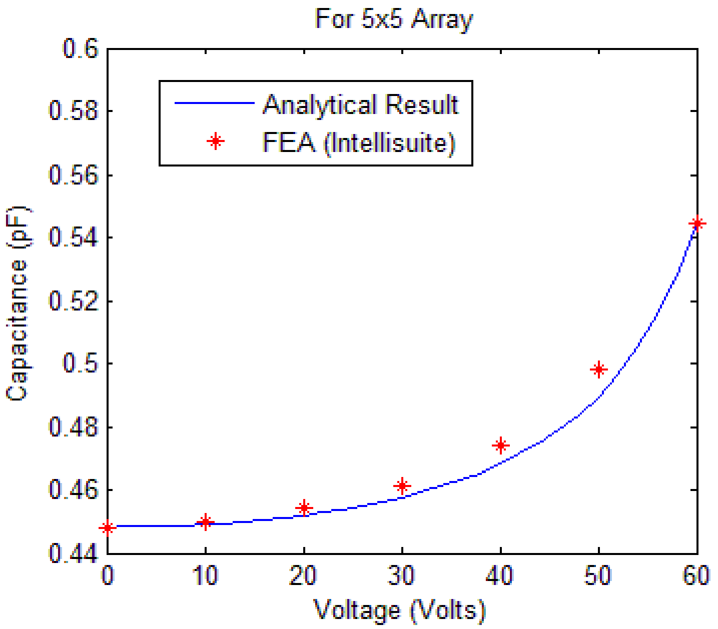

Figure 3.4. Capacitance Vs Voltage

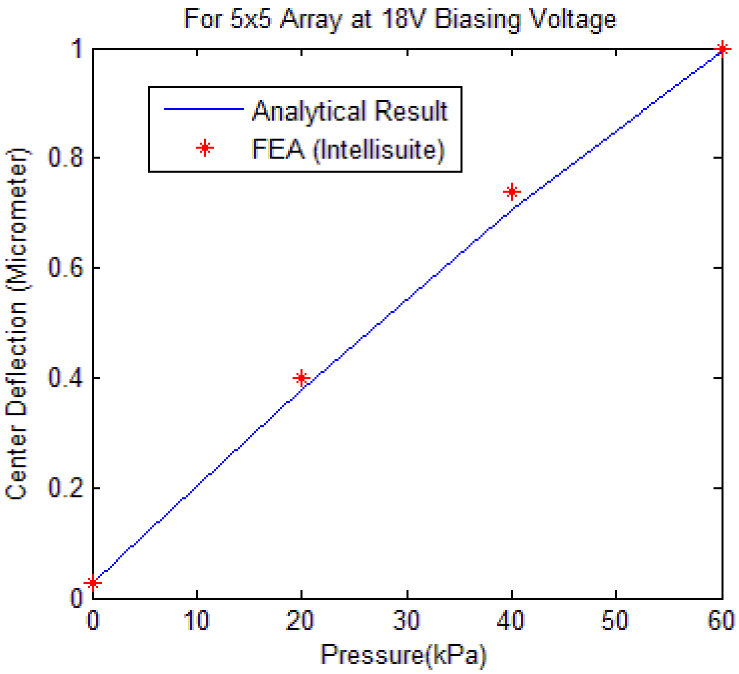

Figure 3.5. Center Deflection Vs Pressure

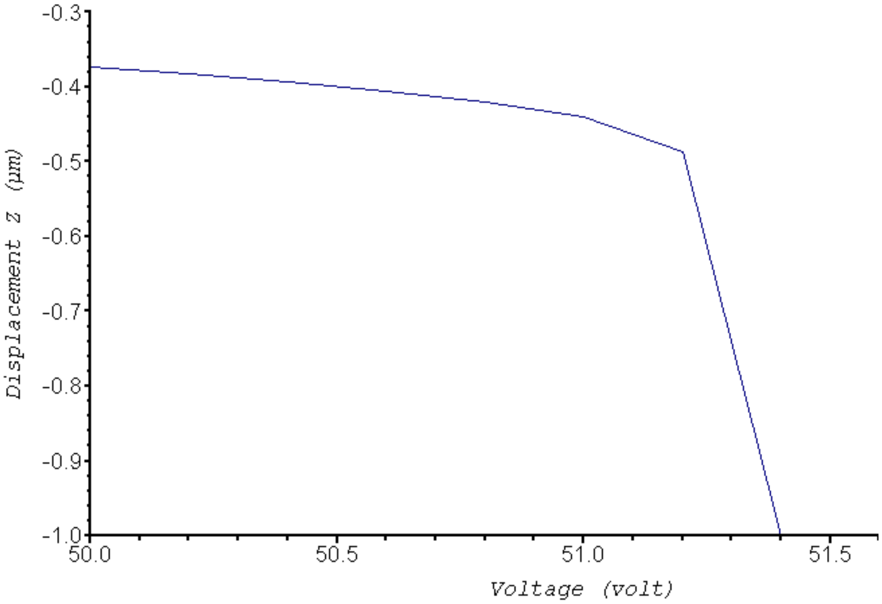

Figure 3.6. Pull-In Voltage Curve obtained from IntelliSuite™ 3-D TEM FEA

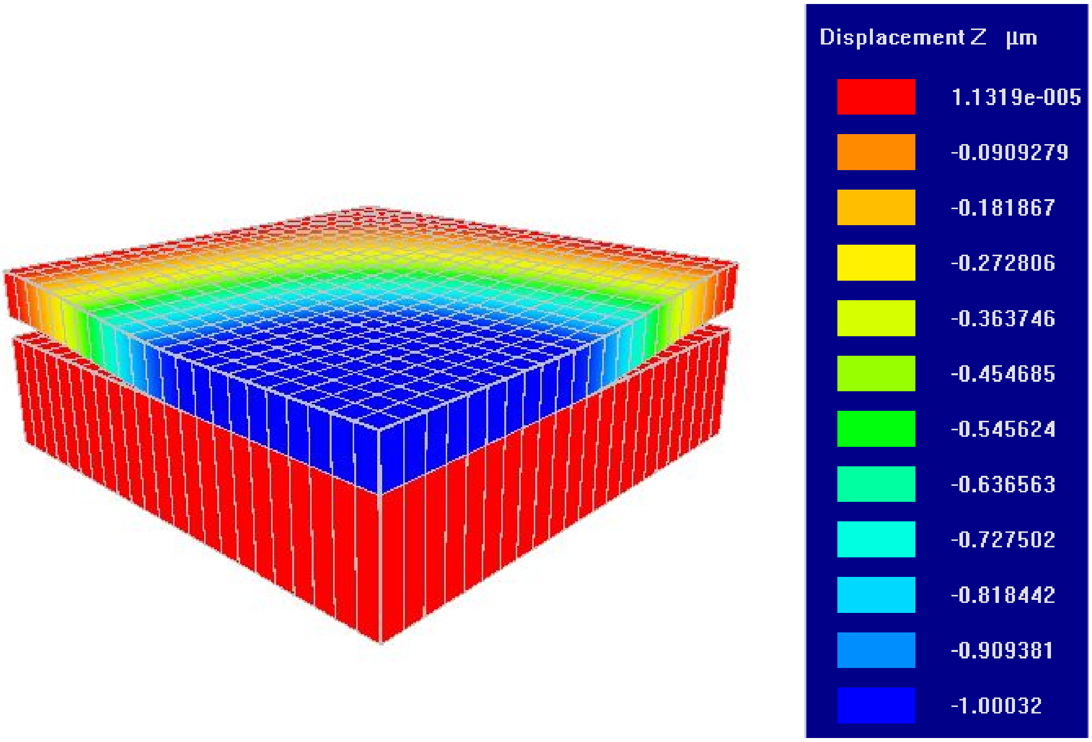

Figure 3.7: IntelliSuite™ Generated Image of Diaphragm at Pull-In

3.5 Beam Shapes

In order to simulate the beamforming capability of the designs, there array factors (as given in chapter two) have been plotted using polar plots. Also to verify the broadband beamforming claim, the beam shapes at various frequencies in the desired range have been obtained. Figure 3.8-3.10 and figure 3.11-3.13 show the beam shapes for design A (7x7 Array) and design B (5x5 Array) respectively. The Matlab code for the same has been provided in Appendix A.

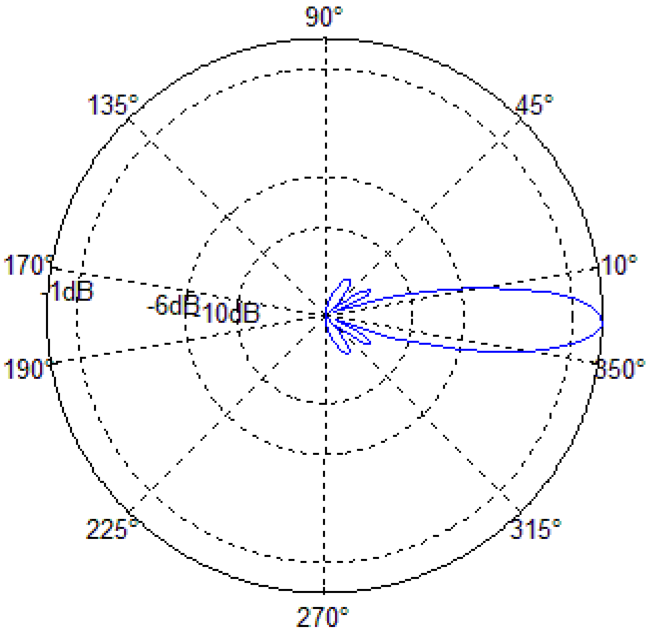

Figure 3.8. 7x7 Array Beam Shape at 113 kHz

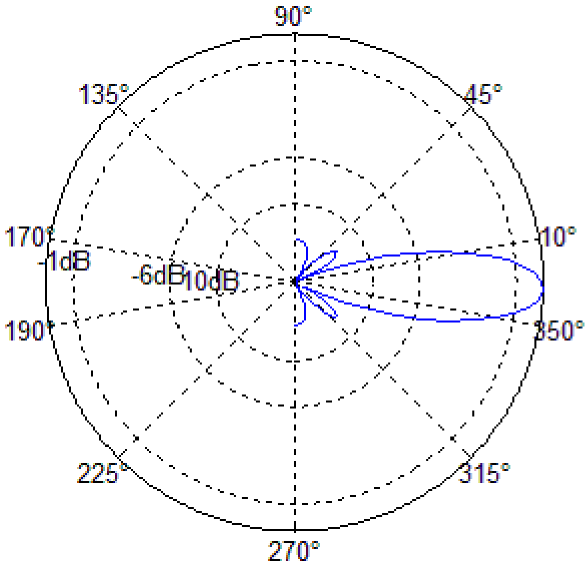

Figure 3.9. 7x7 Array Beam Shape at 140 kHz

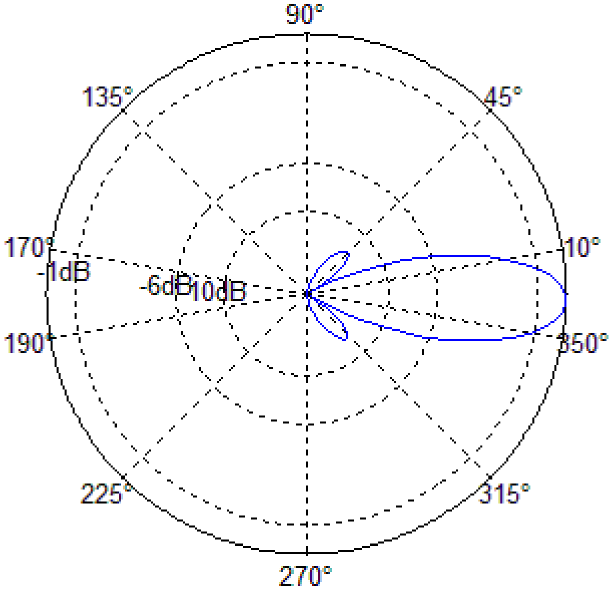

Figure 3.10. 7x7 Array Beam Shape at 167 kHz

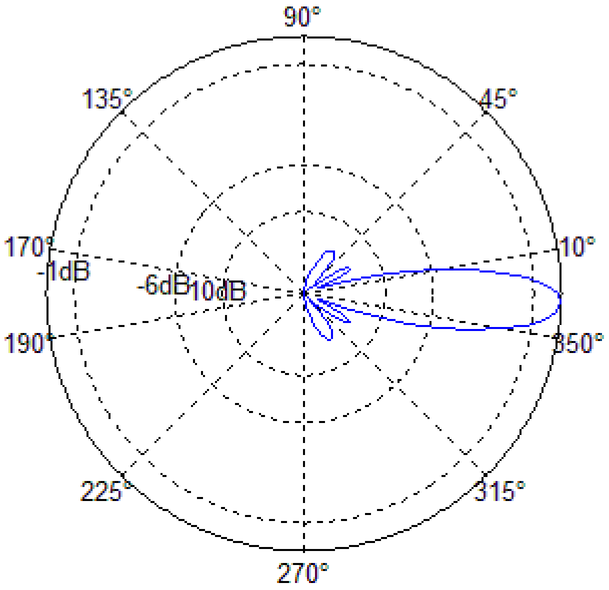

Figure 3.11. 5x5 Array Beam Shape at 113 kHz

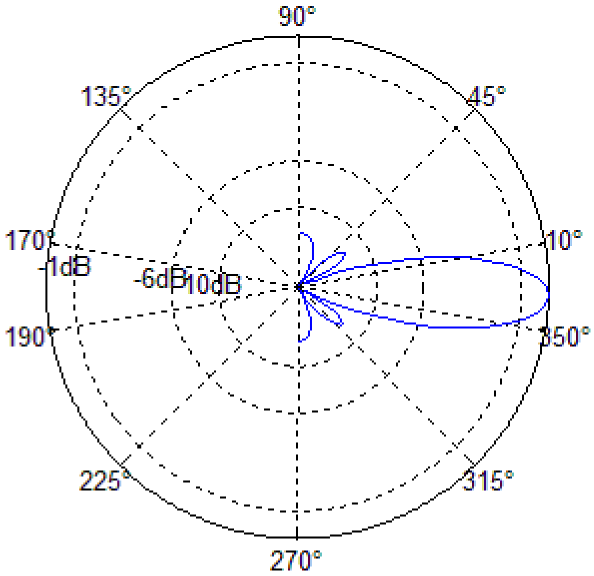

Figure 3.12. 5x5 Array Beam Shape at 140 kHz

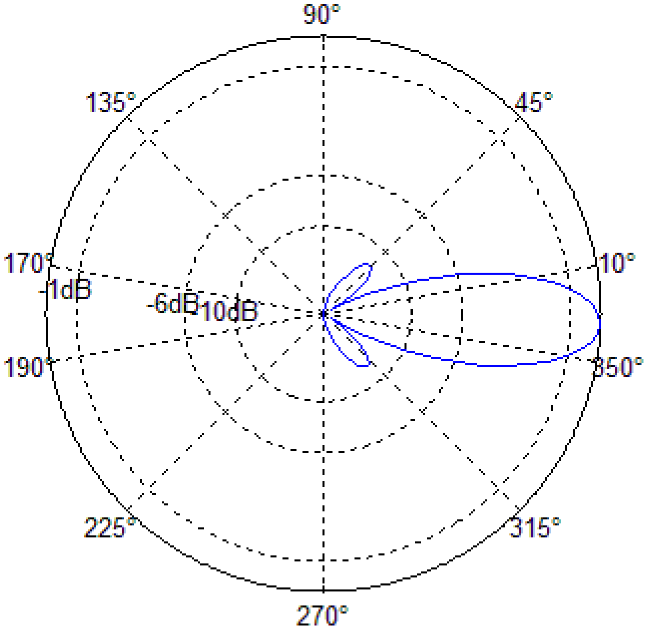

Figure 3.13. 5x5 Array Beam Shape at 167 kHz

Chapter 4

Fabrication

This chapter deals in detail with the fabrication methodology used to fabricate the Capacitive Micromachined Ultrasonic Transducers (CMUT). Each fabrication step description has been provided with the operating conditions, used materials, process type, conceptual cross sectional view and fabrication simulation result from Intellisuite^{TM}. For proof of concept, the fabrication of 5x5 Array was carried out due to its less complex alignment and packaging process. The whole fabrication process was carried out at the Center of Integrated Radio Frequency Engineering (CIRFE), University of Waterloo.

4.1 Array Fabrication Details

An SOI (Silicon-On-Insulator) based fabrication process has been adopted. As compared to other diaphragm material like Si_3N_4 and Polysilicon, the latest SOI based technology has been preferred for the following advantages:

1. Higher switching speeds [25]
2. Higher quality factor
3. Lower value of residual stress
4. Thickness uniformity
5. Reduction in fabrication process complexity

6. Reduction in fabrication steps
7. Lower number of masks
8. Reduction of cost [26]

The microarray has 5 sensing surfaces along each x and y axis. The detailed specification of the SOI wafers used is provided in Table 4.1. The complete fabrication process consists of 8 major steps including dicing. The colors associated with the materials used are shown in fig 4.1.

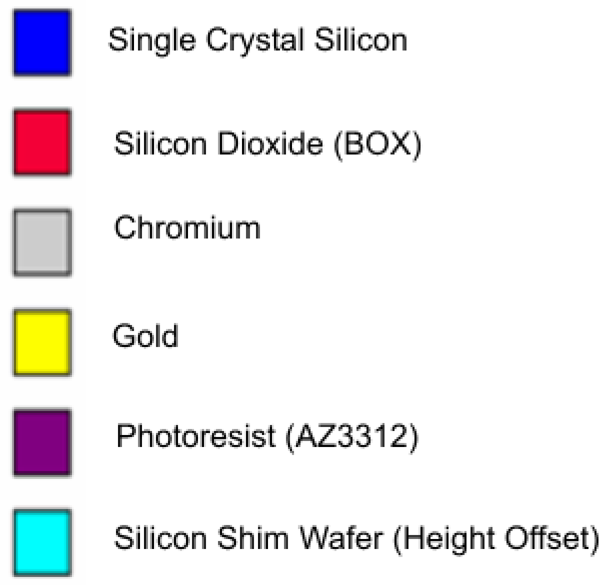

Figure 4.1. Fabrication material legend.

Table 4.1. SOI Wafer Specifications

Parameter	**Specification(s)**
Diameter	150±0.2 mm
Crystal Orientation	<100>
Overall Thickness	352±5 µm
Front side finished	Polished
Back Side Finished	Nanogrind @2000 mesh
Device Layer	
Thickness	2±0.5 µm
Type/Dopant	n/Sb
Resistivity	<0.2 Ohmcm
Handle wafer	
Thickness	350±5 µm
Type/Dopant	n/Phos
Resistivity	<5 Ohmcm
Buried Oxide	
Thermal Oxide	1±5% µm

4.2 Fabrication Process

Step 1: RCA Clean

The wafers are subject to a RCA cleaning before any of the fabrication process can be carried out. The purpose of the cleaning is to remove all organic contamination, oxide film or heavy metal contamination from the wafer. The RCA solution is prepared by adding 130 ml of Hydrogen Peroxide into 600 ml of DI water. Then 130 ml of Ammonium Hydroxide is added to the same sample. The sample is then heated to 70 ± 5^0C using a hot plate. A Teflon holder is used to put the wafer into the solution for 15 minutes. The wafers are then carefully placed under de-Ionized (DI) water tap for approx. 5 minutes so that the RCA solution is flushed out and then dried using a Nitrogen gun [27]. The conceptual, IntelliSuite™ generated and actual photograph has been shown in figure 4.2.

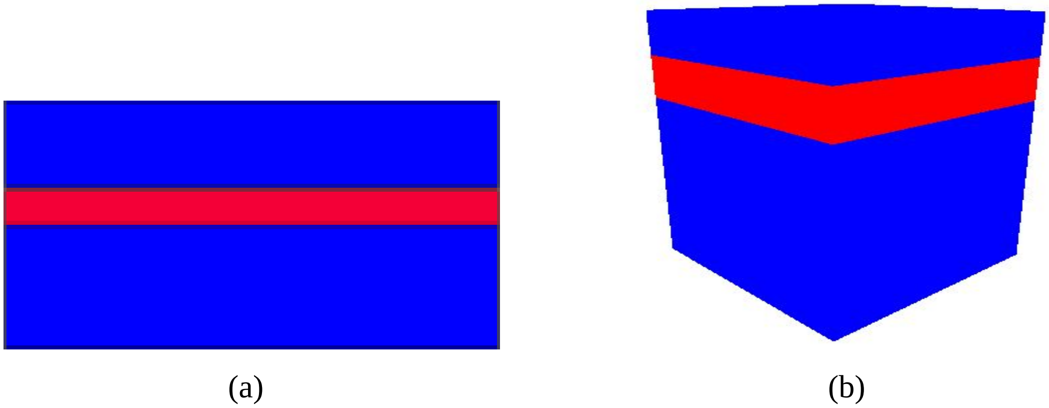
(a) (b)

Figure 4.2. Fabrication step 1 details, (a) Conceptual cross-section and (b) IntelliSuite^{TM} generated 3-D model.

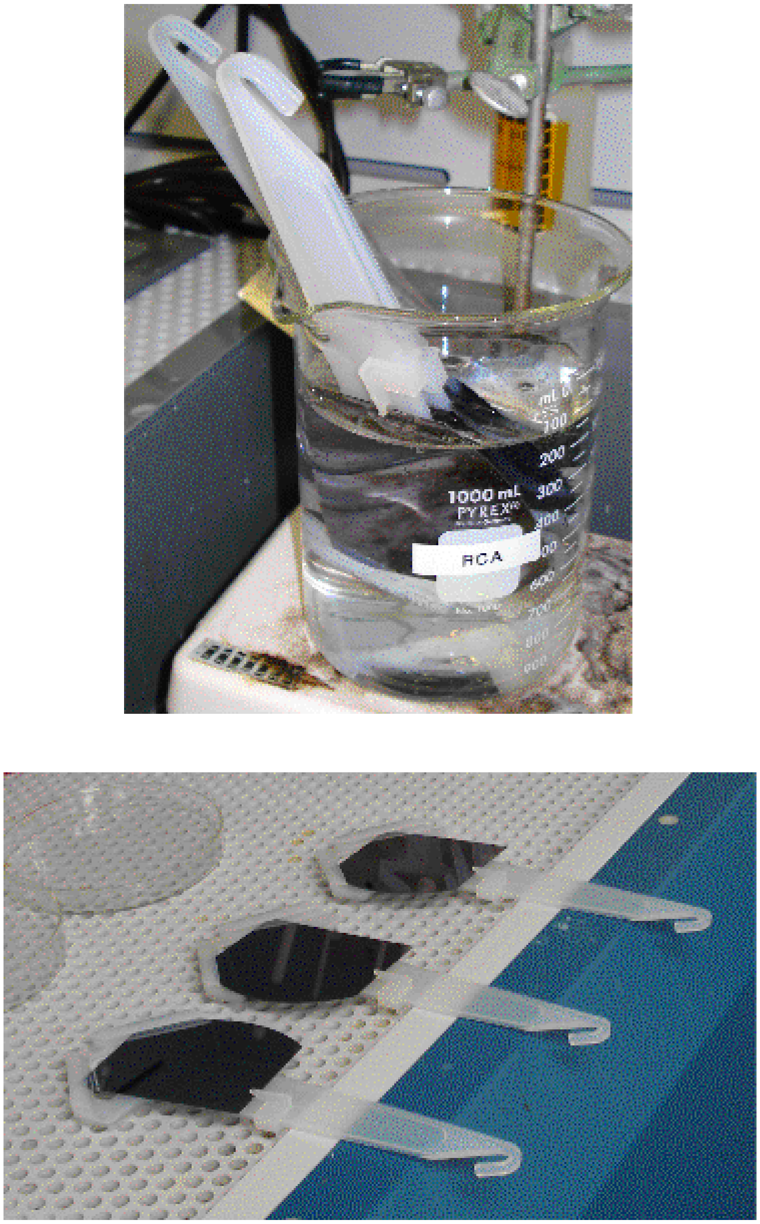

Figure 4.2(c). Actual Picture taken during and after the RCA clean fabrication process steps respectively.

Step 2: Metal Deposition (Gold and Chromium)

The next step after cleaning is to deposit the conductive Gold (Au) layer. Since gold can’t be directly deposited on Si device layer, chromium is first deposited to act as an adhesion layer. A 25 nm layer of Chromium and then 200 nm of gold layer is deposited using electron-beam evaporation method. Intelvac^{TM} Nanochrome deposition system available at the CIRFE clean room is used for the deposition of both chromium and gold. Chromium seed layer was deposited at 20% power which gives a rate of 3.0 Å/sec and Gold conductive layer was deposited at 30% power which gives a rate of 9.2 Å /sec. The two processes are done in one duty cycle in order to avoid oxidation of chromium. The conceptual figure, simulation result and actual fabrication image are shown in figure 4.3 (a)-(c).

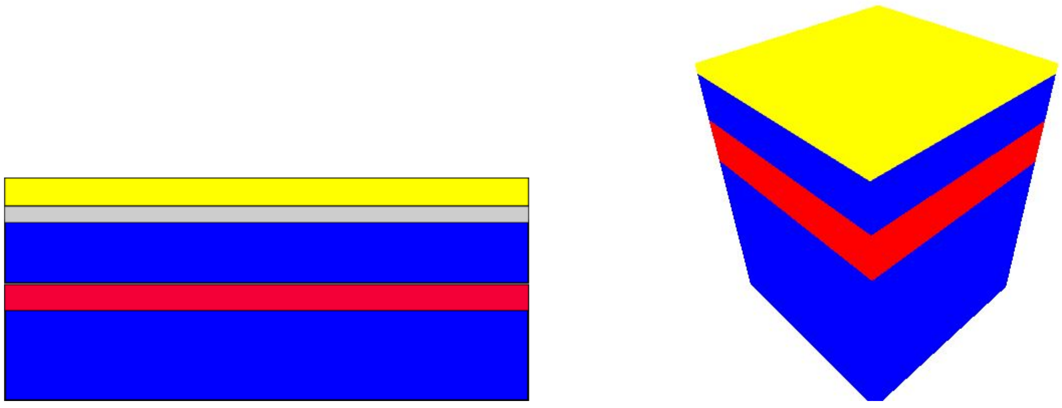

(a) (b)

Figure 4.3. Fabrication step 2 details. (a) Conceptual cross-section, (b) IntelliSuite^{TM} generated 3-D model.

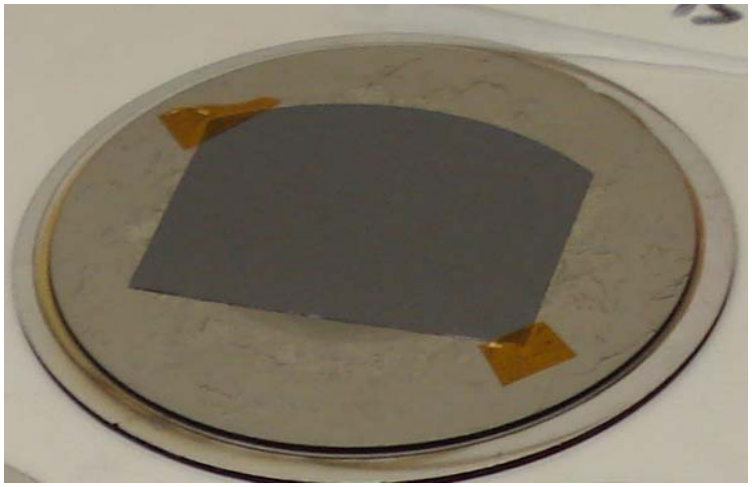

Before

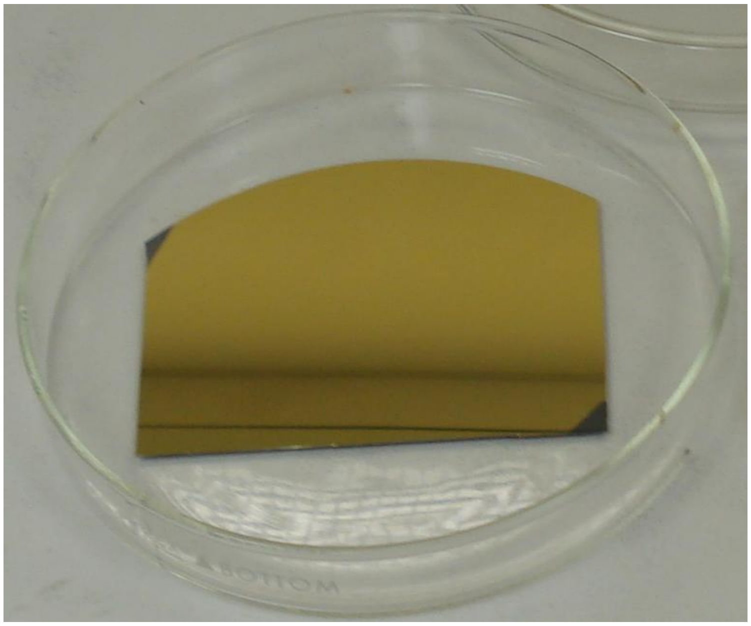

After

Figure 4.3 (c). Actual Picture taken before and after metallization

Step 3: Photolithography

After deposition of conductive metal layer, the next step is to develop a pattern of etch holes on the diaphragm. These etch holes not only provide the route for etching of the buried oxide (SiO_2) but also help in reducing the air damping during diaphragm deflection in receiving and emitting modes. The fabrication constraint allow etch hole dimensions to be at least 15x15 µm separated by a maximum of 30 µm [29]. Taking these constraints into account and optimizing the number of etch holes such that the diaphragm plate is not over perforated to result in a mechanical failure, a 5x5 array of etch hole on each diaphragm were designed as shown below in the fig 4.4(a).

The process of contact photolithography is used to develop the pattern on a positive photoresist AZ3312. This photoresist is spin coated at 3000 rpm for 30 seconds resulting in a thin film thickness of approx 1.0 µm. Then it is pre baked (also known as soft bake) at 90^0C for 60 seconds. This step can also improve the adhesion of the photoresist to the wafer, improve the uniformity of the photoresist layer, and can improve the etch resistance for future processing steps [28]. Soft baking also optimizes the light absorbance characteristics of the photoresist. Soft bake is followed by Ultra-Violet exposure at 41 mW for 9 seconds. The mask used is a chromium mask which can have a minimum feature size of upto 0.5 µm, way more than our limit. The detail drawing of the mask is shown in fig 4.4(b).

After exposure, post-exposure bake of the wafer is carried out for 60 seconds at 90^0C. Post-Exposure treatment is often desired, because the reactions initiated during exposure might not have run to completion. To halt the reactions or to induce new ones, several post-exposure treatments are used. A post-exposure bake may provide more vertical sidewalls compared with a hard

---

bake. This step will also improve the resistance of the photoresist to the developer chemical.

The pattern is then developed using AZ MIF-300 solution by gently stirring it for about 50 seconds inside the solution. Development transforms the latent resist image formed during exposure into a relief image that will serve as a mask for further subtractive and additive steps. During the development process, selective dissolving of resist takes place. The soluble areas of the resist-coated wafer are dissolved by a developer chemical. The pattern is now visible on the wafer. The wafer is then washed with deionized (DI) water and is then dried under a nitrogen gun.

After microscopic examination of the pattern, the wafer is then hard baked at 110^0C for 4 minutes to harden the pattern. The wafer is hard baked in order to evaporate the residual solvents in the photoresist. In addition, this step hardens the resist and prepares the resist for subsequent processing [28].

The images taken after photolithography have been shown in figure 4.4(c) and the dimensions have been verified using an Optical Profiler (Wyko NT1100 series) (figure 4.4 (d)-(e)). The measurement results from the optical profiler show that the etch holes have a side length of 14.7 μm with a separation of 30 μm. This verifies the accuracy of the photolithography and the etching process.

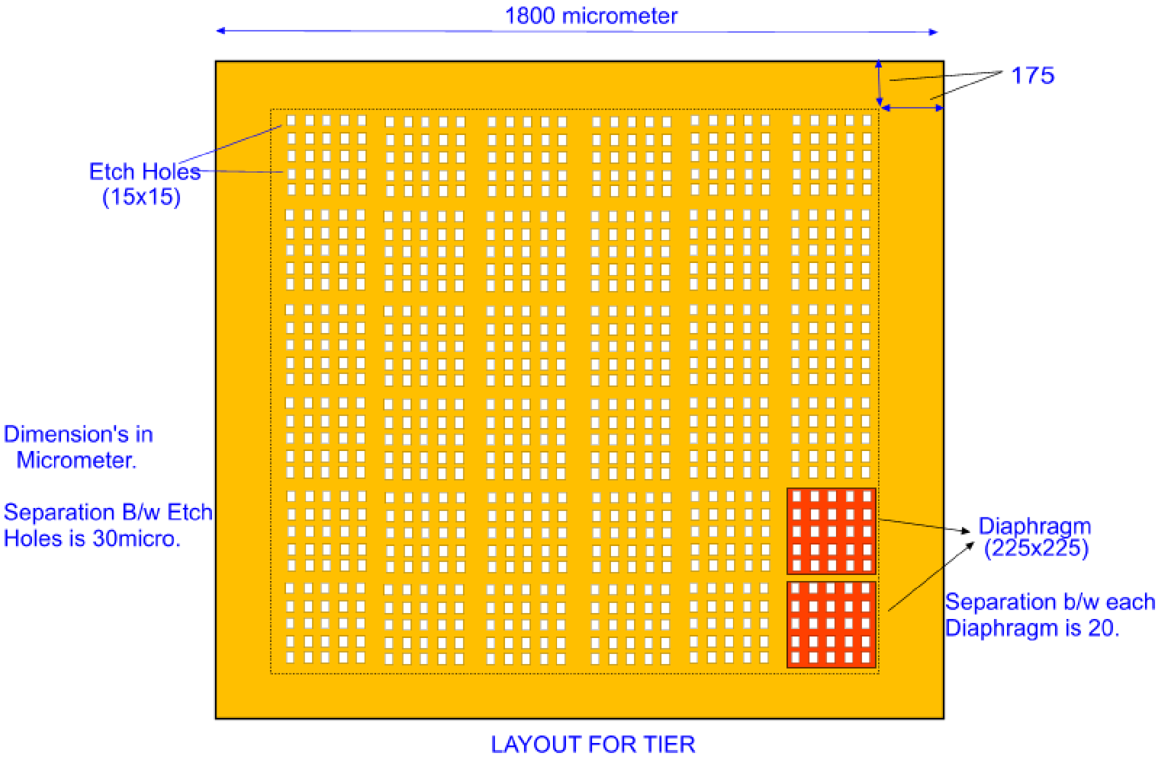

Figure 4.4(a). Single sensing surface details (Conceptual).

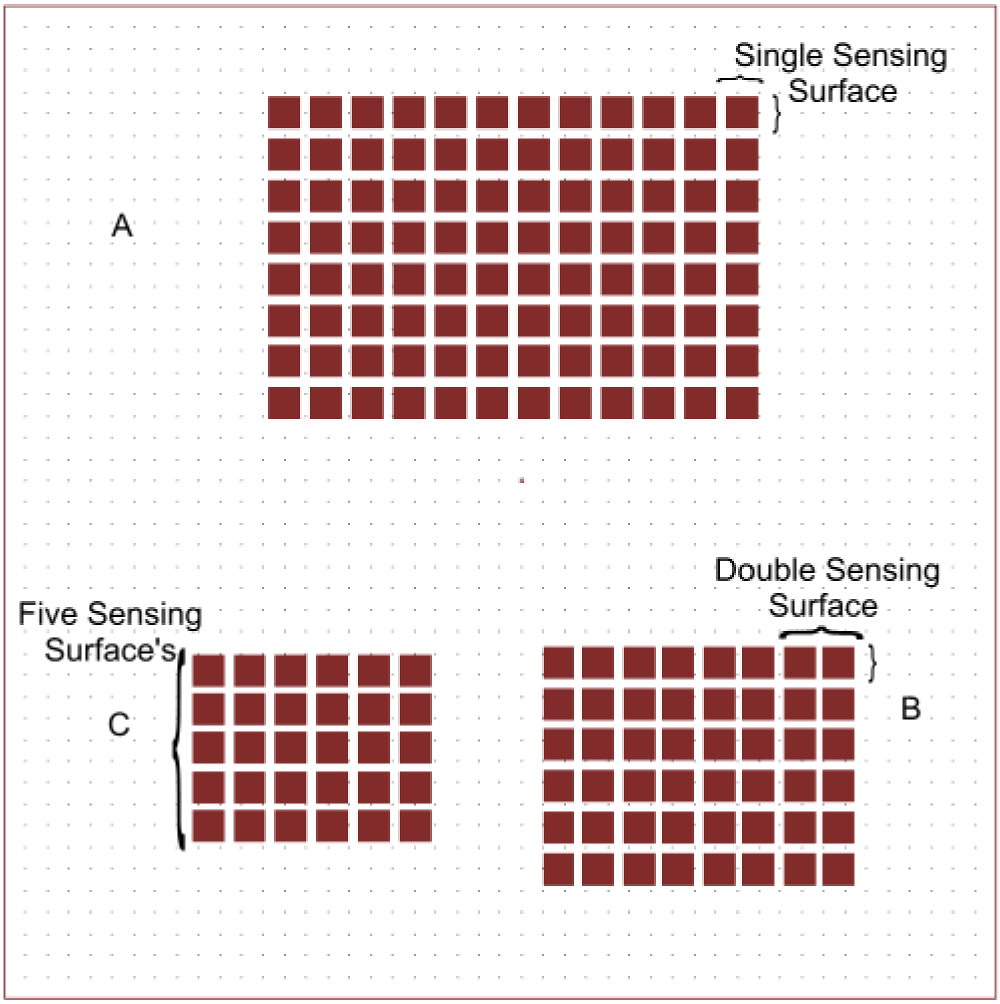

Figure 4.4(b). Complete mask details

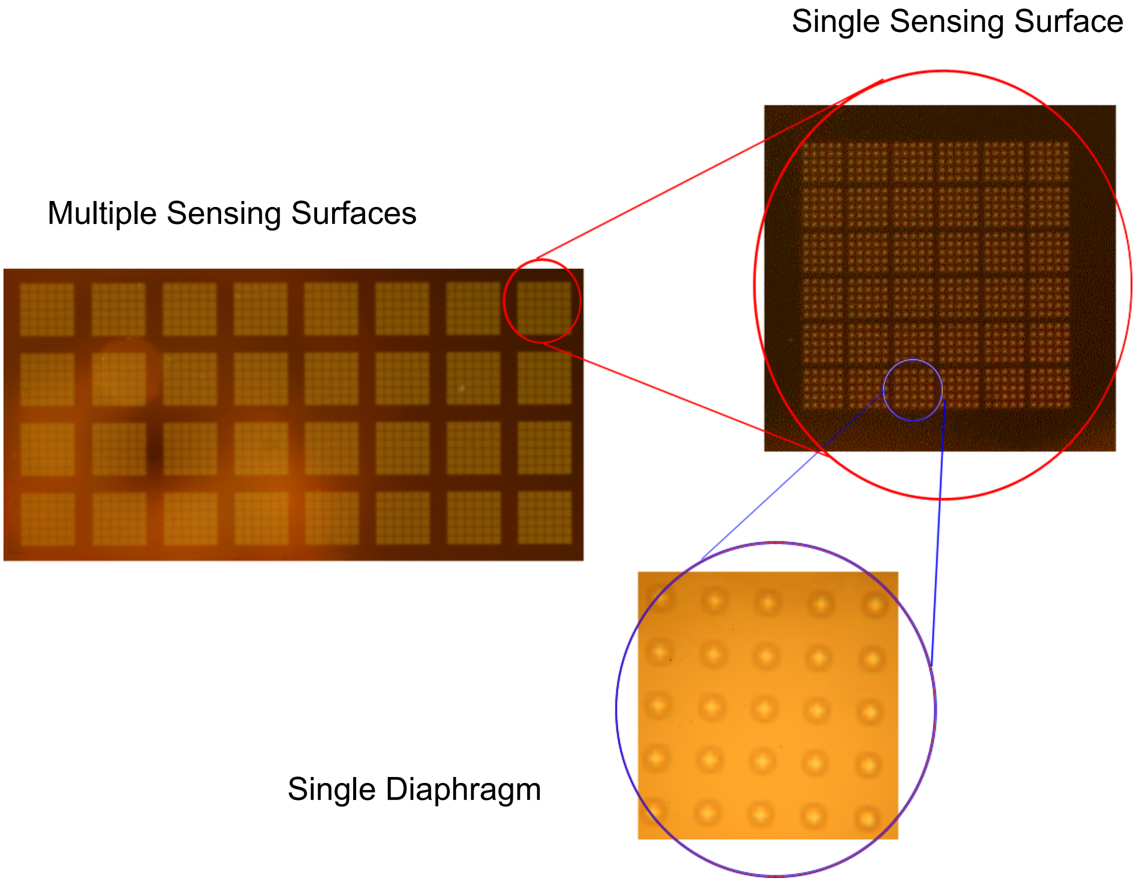

Figure 4.4(c). Images after photolithography.

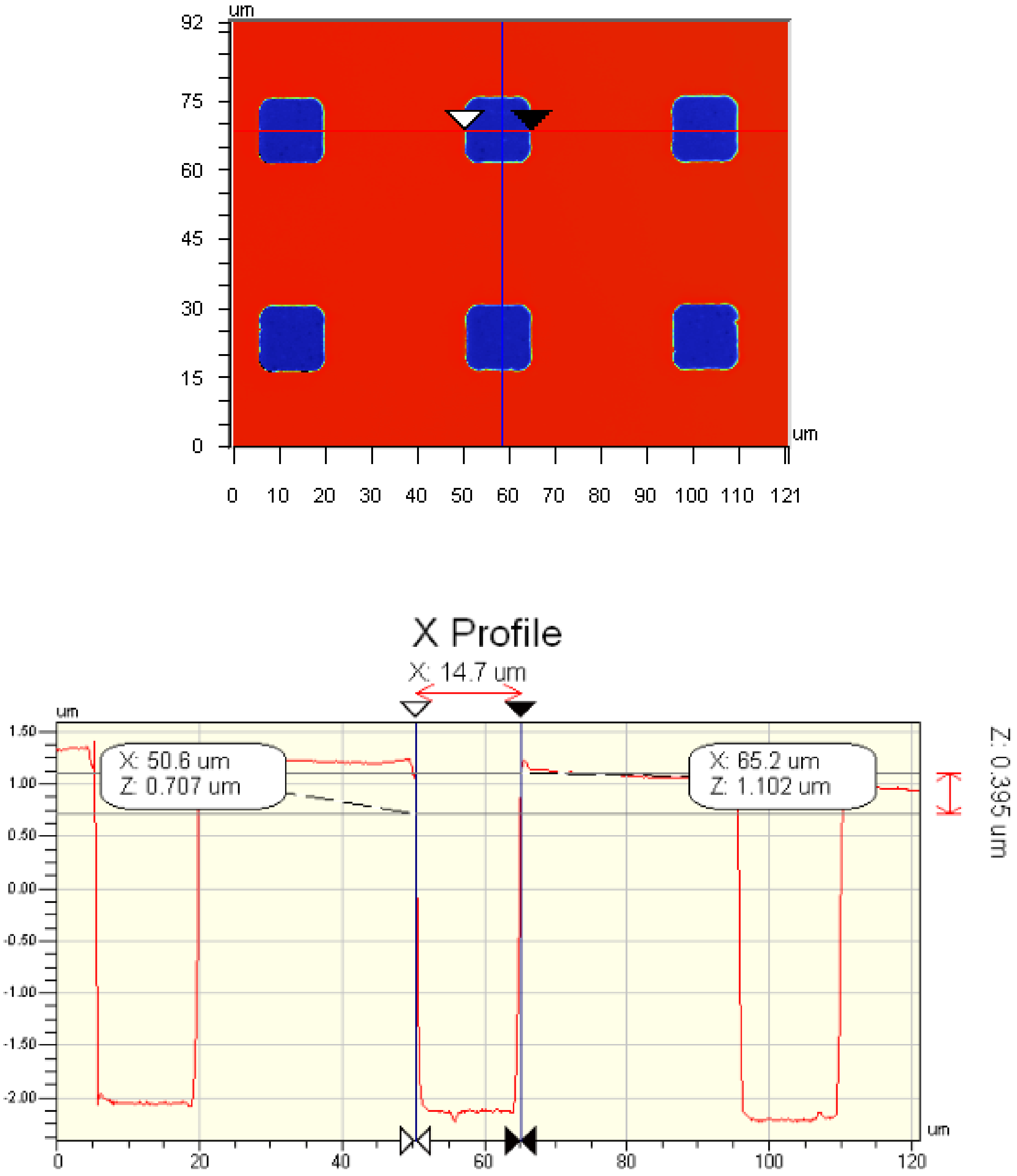

Figure 4.4(d). Optical profiler images (Etch hole dimension).

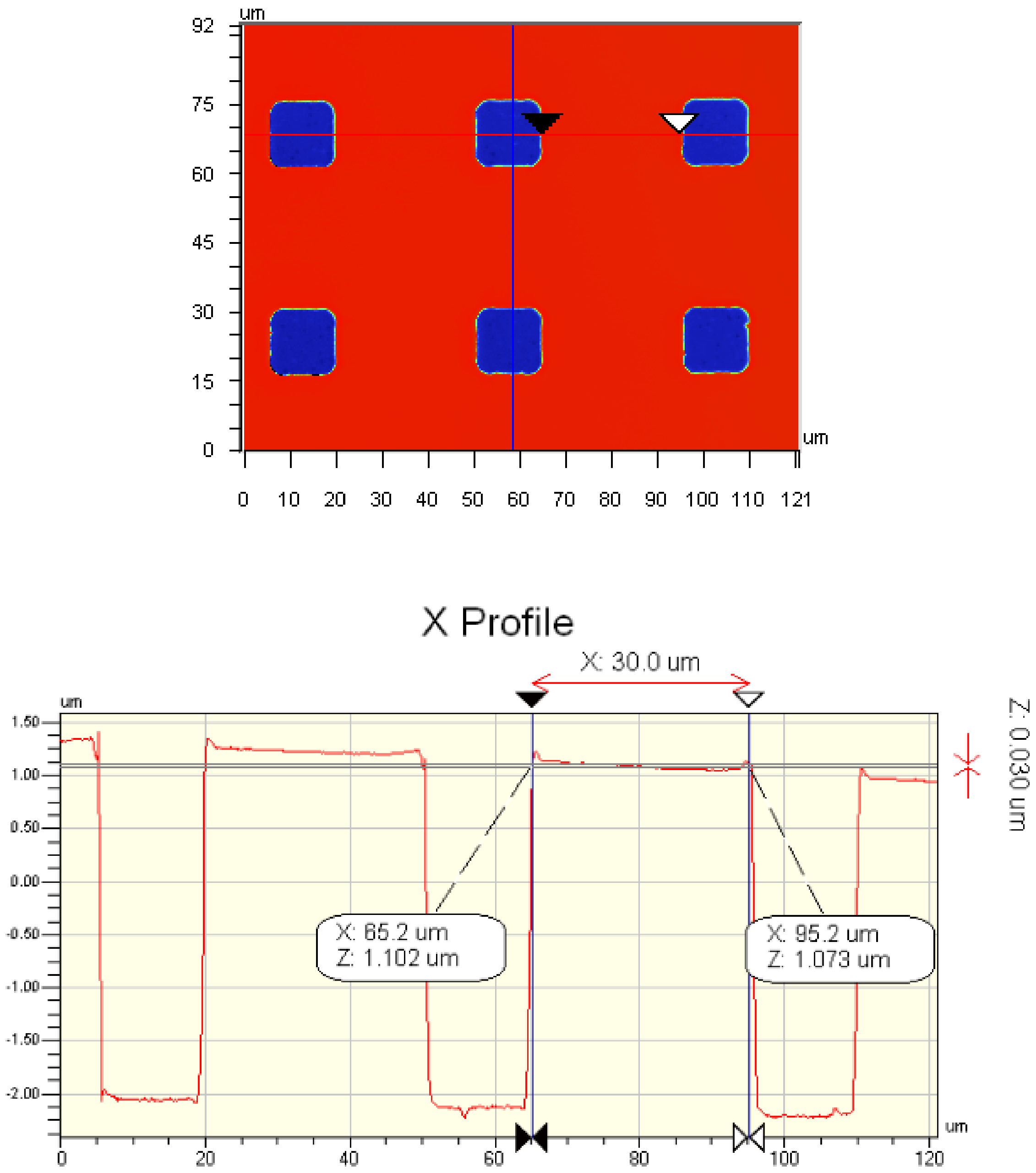

Figure 4.4(e). Optical profiler images (Etch hole separation).

Step 4: Gold and Chromium Etch

After patterning of the AZ3312 photoresist, gold and chromium layers are etched to expose the silicon on the etch holes in the diaphragm. The gold is etched by submerging the wafer in a solution of potassium iodine for 10 seconds at room temperature. The wafer is then rinsed with de-ionized (DI) water. The chromium adhesion layer is then etched by submerging the wafer in a solution of dilute aqua regia (3:1:2 HCl: HNO_3: H_2O) for 10 seconds at room temperature [30]. The pictures of the wafer after gold and chromium etch have been shown below in fig 4.5.

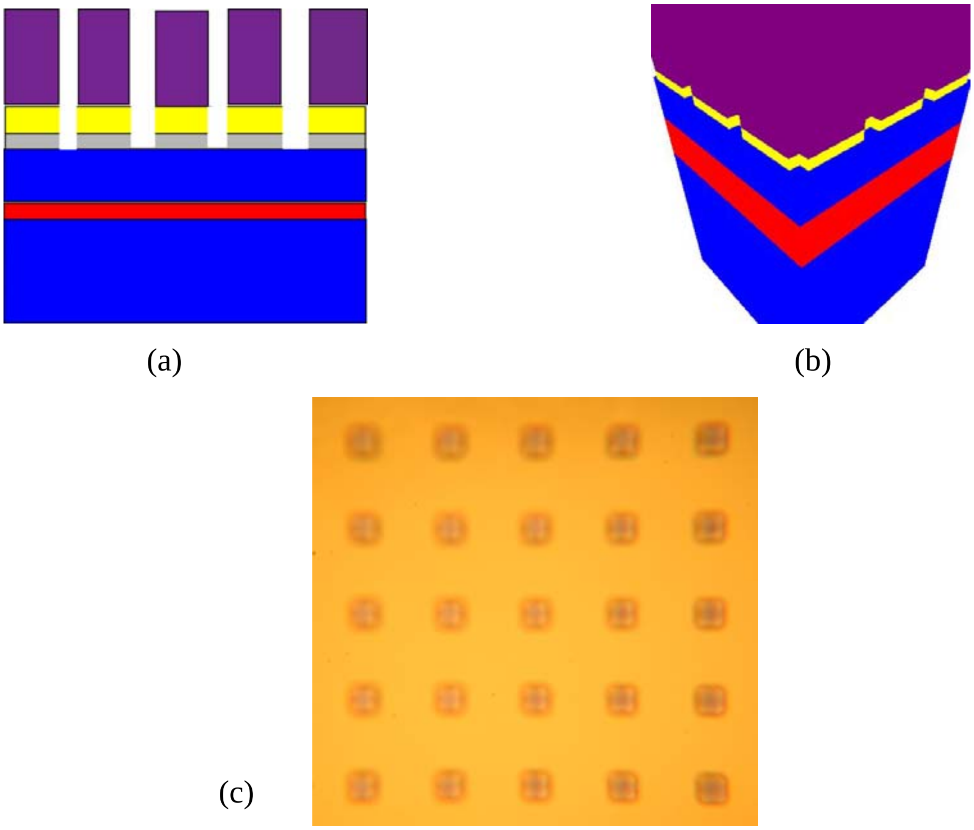
(a)
(b)
(c)

Figure 4.5. Fabrication step 4 details. (a) Conceptual cross-section, (b) IntelliSuite^{TM} generated 3-D model (c) Actual picture taken after metal etch.

Step 5: Silicon Etch

After the Gold and Chromium layer is etched, Silicon at the acoustical ports is exposed for etching. Dry etching of Silicon is done using Reactive Ion Etching process (Trion™ Phantom RIE). After various typical combinations of the recipe were run, it was found that at Inductively Coupled Plasma (ICP) Power of 200 Watts, RF power 25 Watts Pressure 50 mtorr, SF_6 25 sccm and O_2 5 sccm the etch rate is appreciable and isn't damaging the masking layers of photoresist as well as Gold and Chromium layers. Higher value of ICP is used to attain higher etch rate and hence to avoid longer stay of sample in the chamber. RF power is used to keep the etching more anisotropic. The results after Silicon etch is shown below in fig. 4.6 (a)-(c). The measurement results obtained from optical profiler verifies that the silicon has been etched as the depth of the etch holes is more than that of the silicon device layer.

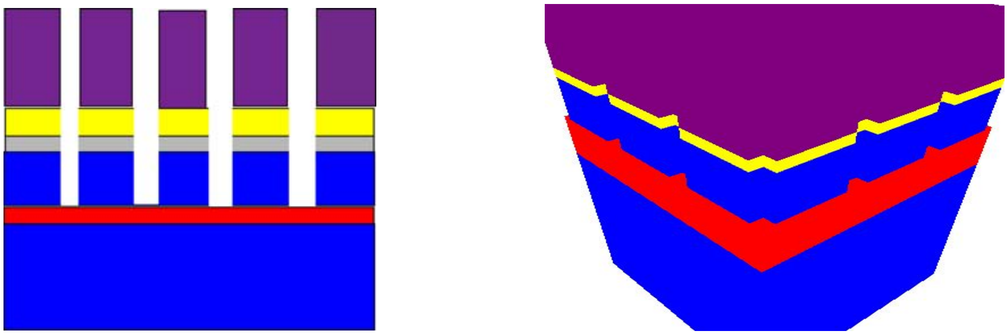
(a) (b)

Figure 4.6. Fabrication step 5 details. (a) Conceptual cross-section, (b) IntelliSuite^{TM} generated 3-D model.

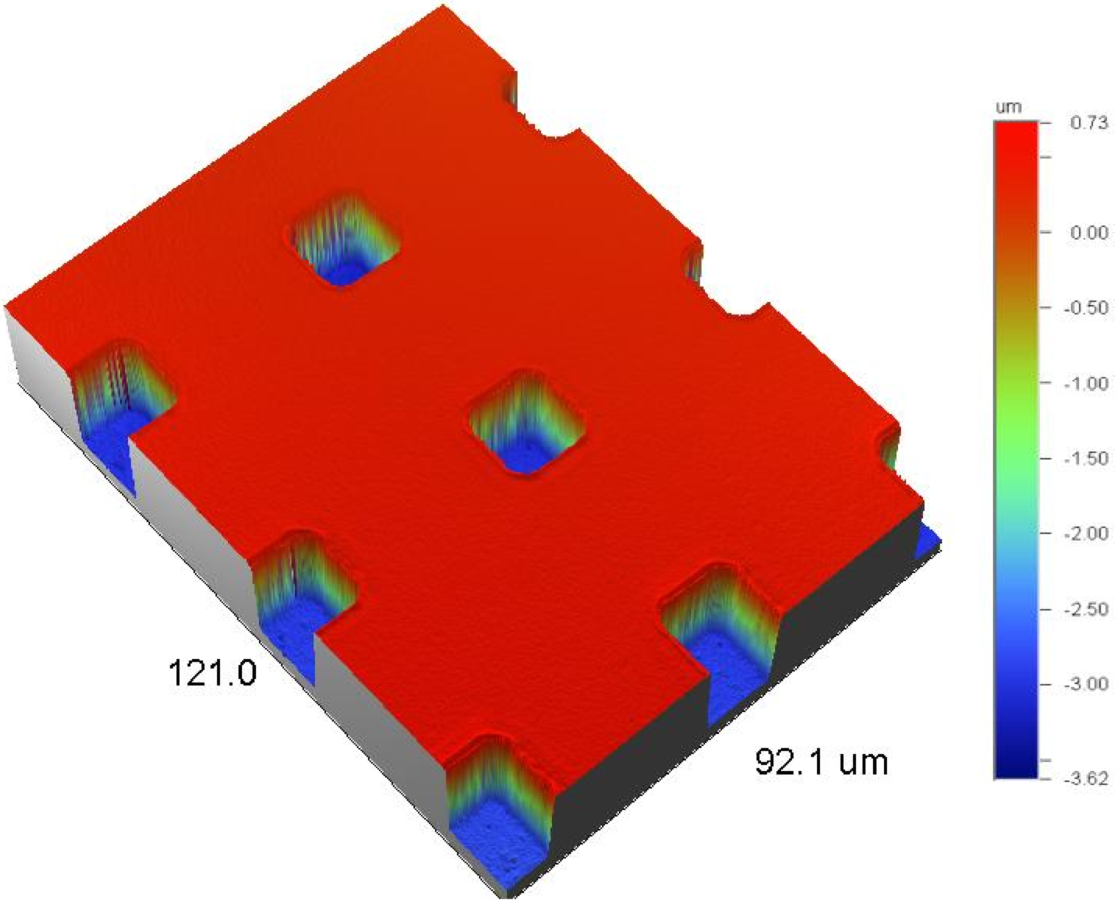

Figure 4.6 (c). Optical profiler Images after Silicon etch (RIE).

Step 6: Dicing and Photoresist Removal

After the silicon has been etched and the devices are ready for release, it is important to get the individual dies separated. This is done in order to avoid the released devices from being exposed to the heat, pressure and water-jet thrust during the dicing which may break the erstwhile released devices. The photoresist layer is also stripped after the dicing process to protect the device layer and to help in cleaning the dicing chip's afterwards. Once the dicing is done using the K&S 780 Dicing Saw (NanoFab, University of Western Ontario), the dies are places in Gelpak^{TM}. This is followed by stripping off the photoresist (AZ3312) using KWIK Strip solution. The dies are placed in KWIK Strip solution for 2 hours at 65^{0}C and then in Isopropyl Alcohol (IPA) solution followed by deionized water [28]. The process has to be carried out with utmost care because of the small size of the dies. Once the dies are taken out from the DI water they are dried on napkins and place back in Gelpaks^{TM}. The pictures of individual dies are shown below in fig 4.7.

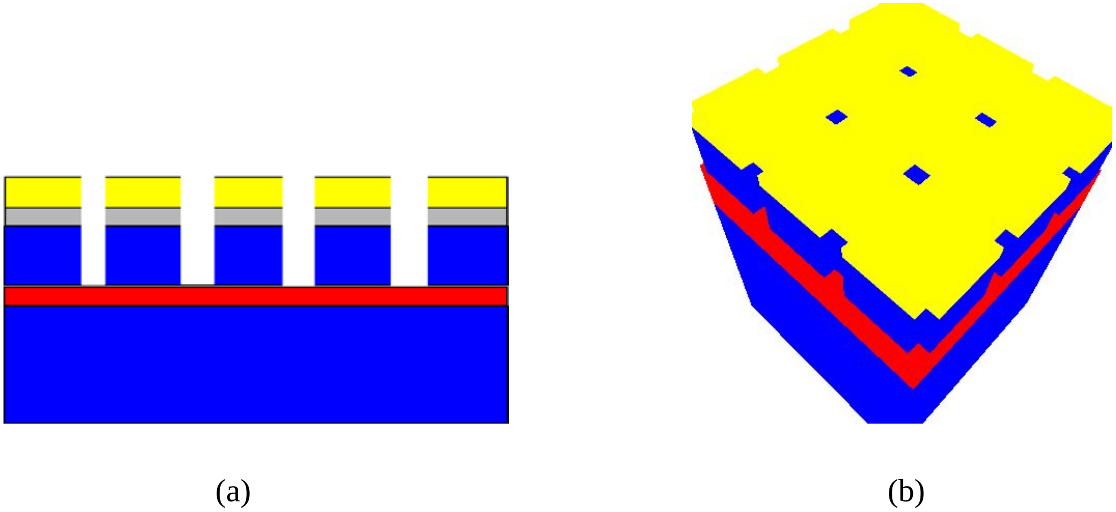
(a) (b)

Figure 4.7. Fabrication Step 6 details. (a) Conceptual cross-section, (b) IntelliSuite^{TM} generated 3-D model.

Step 7: Release and Critical CO_2 Drying

After dicing, the diaphragms have to be released by etching the buried SiO_2. It is important to note that SiO_2 is an amorphous material which etches equally well in all directions (isotropic etching). The most commonly used etchant is aqueous hydrofluoric acid (HF) solution, because of its high selectivity between Si/SiO_2. The chemical mechanism involved is given by the following equation below:

$$SiO_2\ (s) + 4HF\ (aq) \rightarrow SiF_4(g) + 2H_2O$$

The most common form of the HF solution used is 5:1 Buffered Hydrofluoric (BHF) solution, but it gives lower etch rate and would have required more than 3 hours to etch the required SiO_2 [30]. This prolonged exposure of metal layer to BHF could have affected the metal layer. In order to avoid this 49% HF solution was used which has a very fast etch rate, about 2.3 μm/min for thermally grown SiO_2, which is harder to etch. After being placed in 49% HF solution for 5 minutes 30 seconds, the dies are gently moved to a deionized (DI) water bath. One significant technological problem in surface micromachining is the unintended adhesion of released mechanical elements to the substrate. When using a wet release etch, the surface tension during drying can pull compliant structure (beams or diaphramgs) into contact with the substrate, and during the final drying, they can adhere firmly together. This phenomenon is generically called stiction. Methods of avoiding stiction include [19]:

1. Use of Self-Assembled molecular monolayers (SAM'S) to coat the surfaces during the final rinse with a thin hydrophobic layer, reducing the attractive force,

2. Use of Vapor or dry-etching release methods, such as XeF_2,
3. Various drying methods (freeze drying and drying with supercritical $C0_2$) that remove the liquid without permitting surface tension to act, and
4. Temporary mechanical support of the moveable structure during release using posts of photoresist or some other easily removed material.

After the dies are released, Supercritical CO_2 drying was carried out to avoid stiction of the devices. This was done using the Tousimis Automegasamdri-915B, Series C Critical Point CO_2 Dryer, available at CIRFE, University of Waterloo. Supercritical CO_2 drying process allows samples to be dried without any surface tension, thus reducing the likelihood of stiction. This process is typically used to dry samples that have been rinsed in de-ionized water. The de-ionized water is replaced by methanol prior to the drying process, and then the methanol is displaced by liquid CO_2 as part of the drying process. Before the dies can be placed inside the CO_2 dryer chamber, the dies should be placed in isopropyl alcohol (IPA) baths for 8 minutes and this step should be repeated at least three times [31]. Figure 4.8 shows the conceptual, IntellliSuite simulation and actual photograph of a sensor after the diaphrams are released.

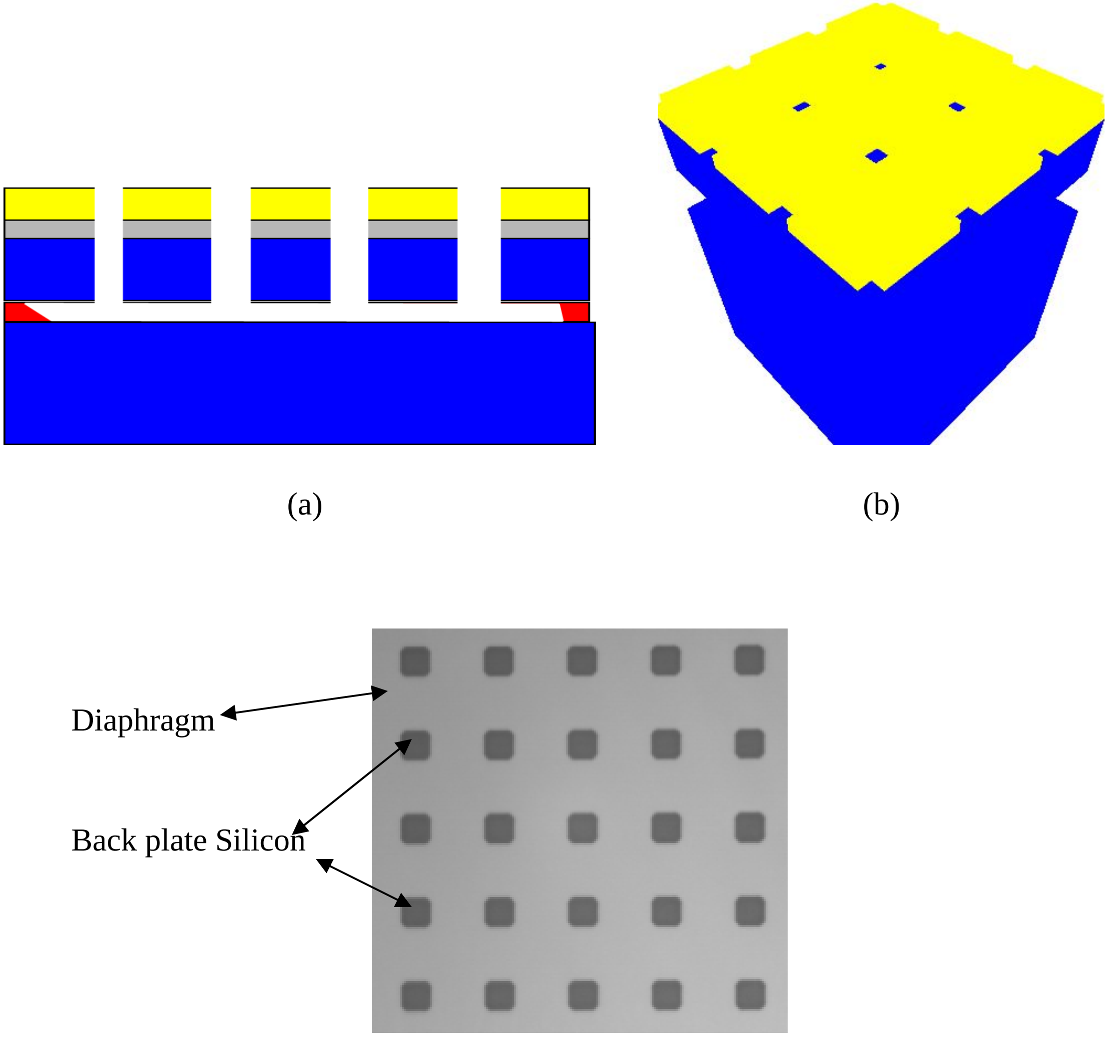

(a) (b)

(c)

Figure 4.8. Fabrication Step 7 Details. (a) Conceptual cross-section, (b) IntelliSuite^{TM} generated 3-D model (c) Actual Image after release.

Chapter 5

Assembly and Packaging

This chapter presents the assembly and packaging details of the Non-Planar Capacitive Micromachined Ultrasonic Transducer (CMUT) Array. After the fabrication and dicing of the CMUTs, they are then assembled using shim or dummy silicon wafers to obtain proper vertical offset to realize the desired discretized hyperbolic paraboloid geometry. After assembling, individual sensing surfaces are electrically connected to the bonding pads of a commercially available PGA-68 package using gold bonding wires. The assembling and packaging of the final array geometry was carried out with the help of AdvoTech™ Company Inc., U.S.A.

5.1 Assembly Details

Since state-of-the-art microfabrication processes are basically planar in nature as discussed in chapter four, the individual sensing surfaces were fabricated as planar devices as discussed in chapter 4. The individual sensing surfaces are to be assembled in proper orientations and at proper height offsets to obtain the shape of a discretized hyperbolic paraboloid geometry.

Silicon shim wafers or dummy wafers are used to obtain the necessary height offset for the individual dies (sensing surfaces). To obtain different height offsets, multiple shim wafers are used each of which has a thickness of 350 µm. This value has been obtained by dividing the total array height with total number of discrete elevations in case of a 5x5 array. To attach the SOI based sensing surface to the shim wafers underneath, a conductive silver filled epoxy is used. Conductive epoxy is used to provide a conductive connection between the handle layer of SOI base CMUT and the Silicon shim wafer so that a common electrical base point is obtained for all the dies instead of having separate grounding for each of them. This also helps in reducing the pin connection complexity. Another factor to be addressed here is that the vertical offset should keep proper isolation between the two different voltage levels, which is the biasing voltage and the ground level. At the top right corner of the lower level CMUT, which is at biasing potential, there is a risk of potential electrical short circuit with the base plate as shown in figure 5.1(a). To overcome this problem another vertical coating of non-conducting adhesive has been used, as shown in Figure 5.1(b).

The deposition of conductive and non-conductive adhesive on vertical and horizontal side respectively has been carried out using Micro Alignment set up with the help of AdvoTech™ Company Inc., U.S.A.

Figure 5.1(c) shows the Silicon shim wafer (Height Offset) assembled inside a PGA-68 package. Figure 5.1(d) and (e) shows the side view and the top view of the sensing surface arranged on top of Silicon shim wafer. The Capacitive Micromachined Ultrasonic Sensors are place on top of this using the above described process and then connected to the package as described in the next section.

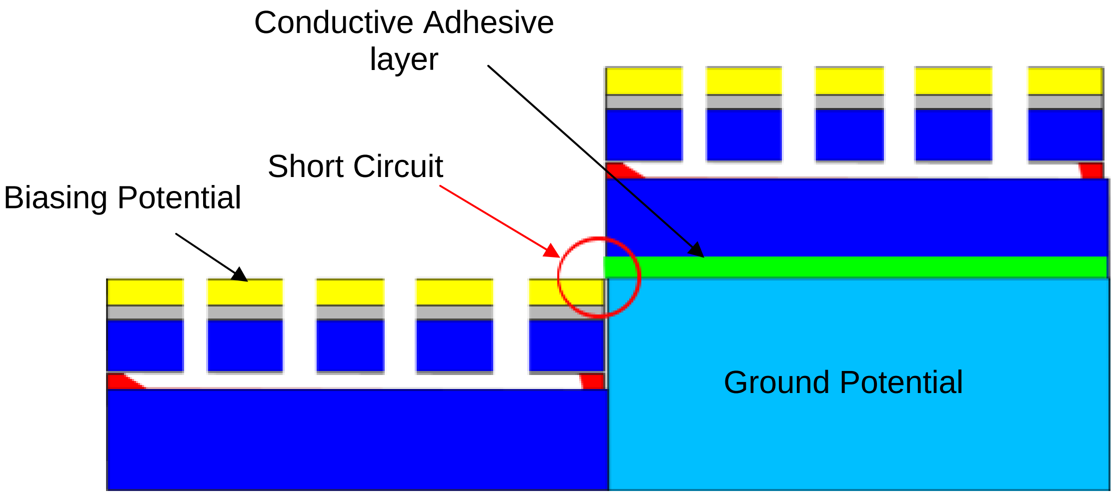

Figure 5.1(a). Illustration of assembling and short circuit condition.

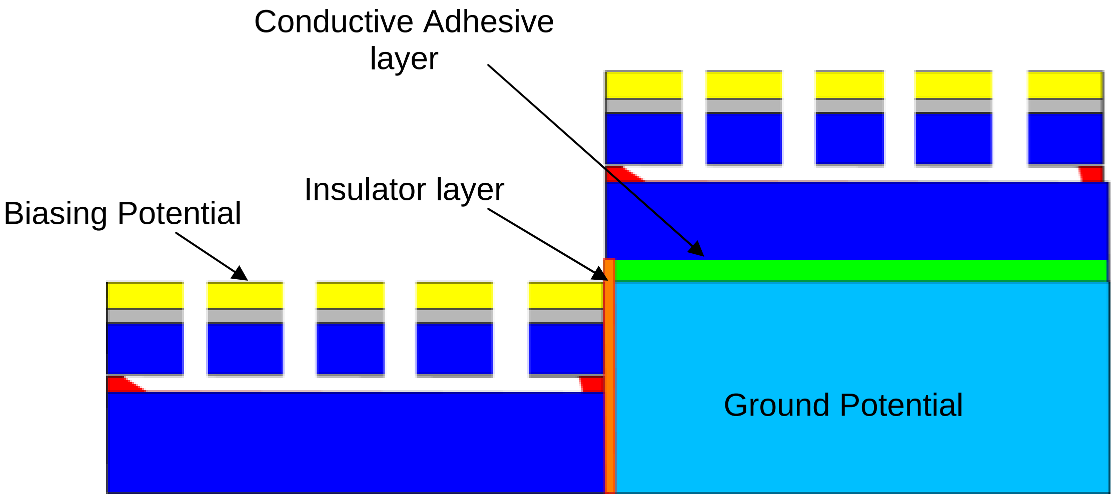

Figure 5.1(b). Illustration after non-conductive vertical coating.

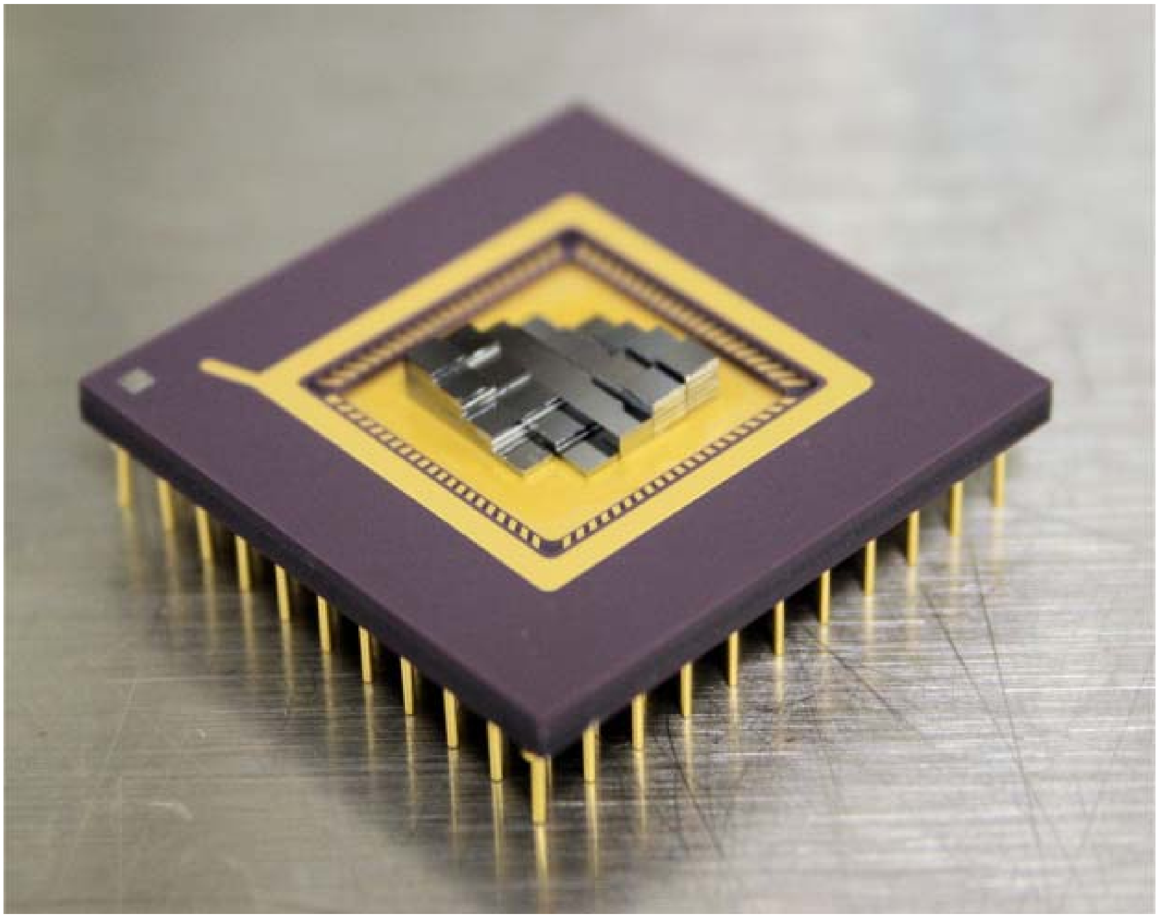

Figure 5.1(c). Illustration of silicon shim wafer Inside a PGA-68.

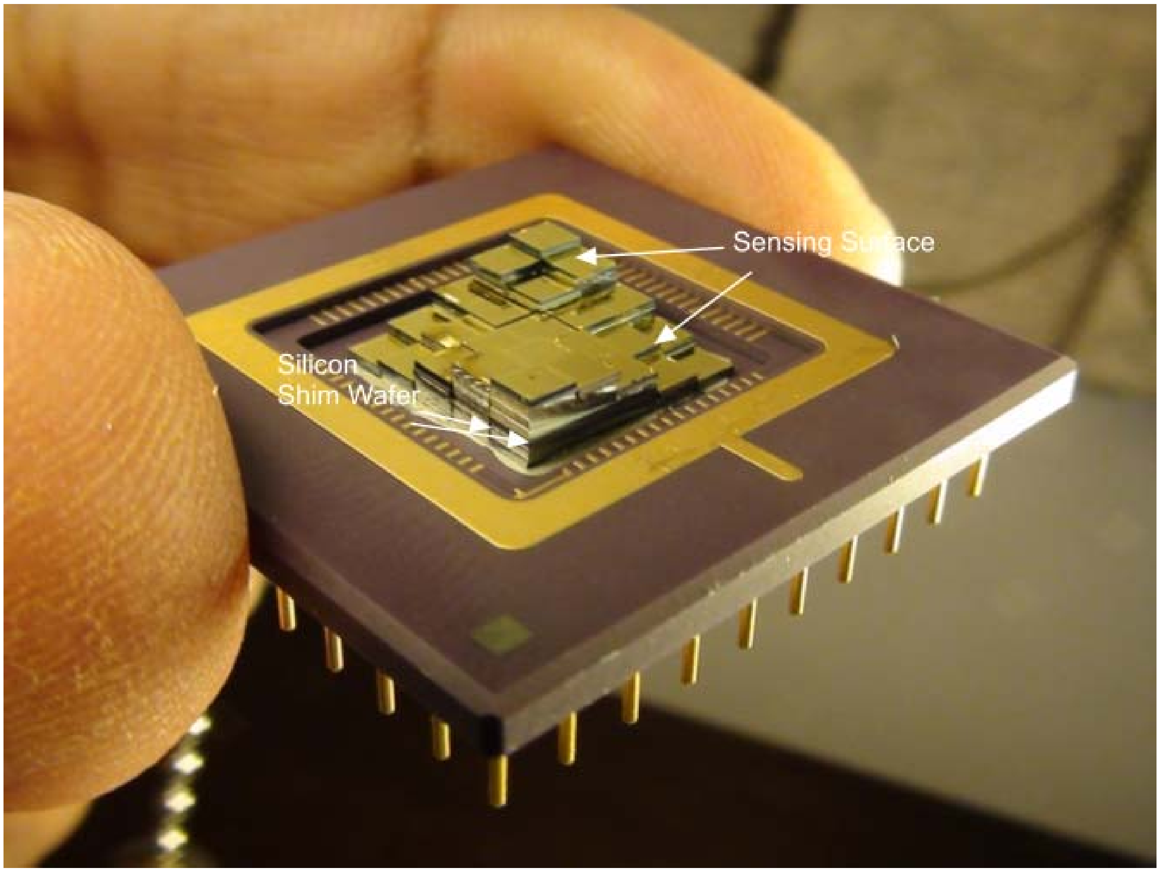

Figure 5.1(d). Illustration of sensing surface over a silicon shim wafer (Side view).

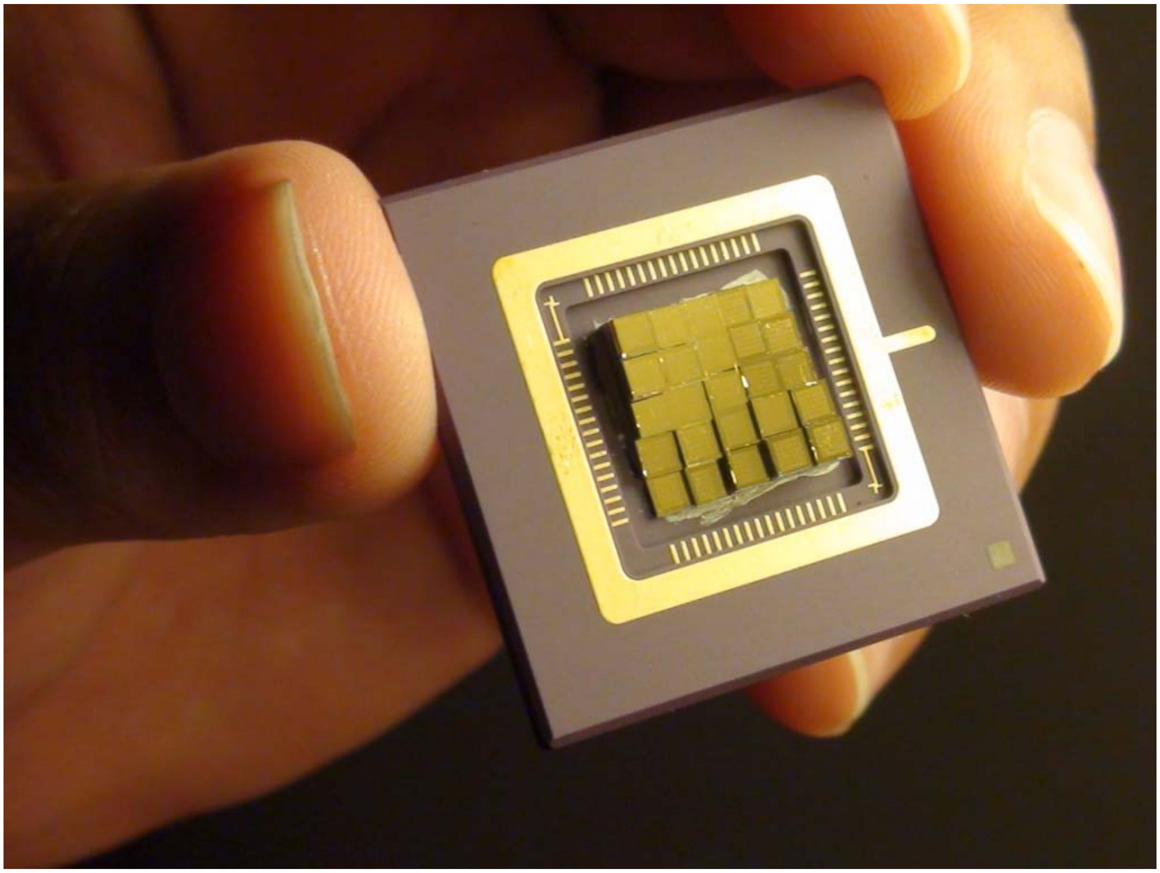

Figure 5.1(e). Illustration of sensing surface over a silicon shim wafer (Top view).

5.2 Packaging Details

The package serves to integrate all of the components required for a system application in a manner that minimizes size, cost, mass and complexity. The package provides the interface between the components and the overall system. The three main functions of the MEMS package are mechanical support, protection from the environment, and electrical connection to other system components [32].

The array has a dimension of 9.0x9.0 mm and a PGA-68 package has a cavity size of 12.0 x 12.0 mm that can accommodate a maximum die size of 10.2x10.2 mm. Thus a commercially available PGA-68 package will meet the requirements for the CMUT microarray. This detail was confirmed with Canadian Microelectronic Corporation (CMC Microsystems). Figure 5.2 shows the PGA-68 package details. Another requirement of packaging is the definition of bonding pads. In order to ease the assembly and interconnection process while avoiding the orientation issue, each of the sensing surfaces has been fabricated to have a 175 µm wide symmetrical bonding ring (as shown in figure 4.4(a), chapter Four). Thus the gold bonding wires can be bonded at any location on the symmetric bonding pad.

The pin connection details of a PGA-68 package are shown in Table 5.1. A pictorial presentation of the pin connection is also presented in figure 5.3. The connection chart has been made considering the bonding tail and bonding pitch factor and also the redundancy in case of longer connections with interior dies, for example die A3 as shown in figure 5.3.

The actual device after complete Assembling and Packaging has been shown in Figure 5.4 and 5.5. The device is now complete and ready for testing.

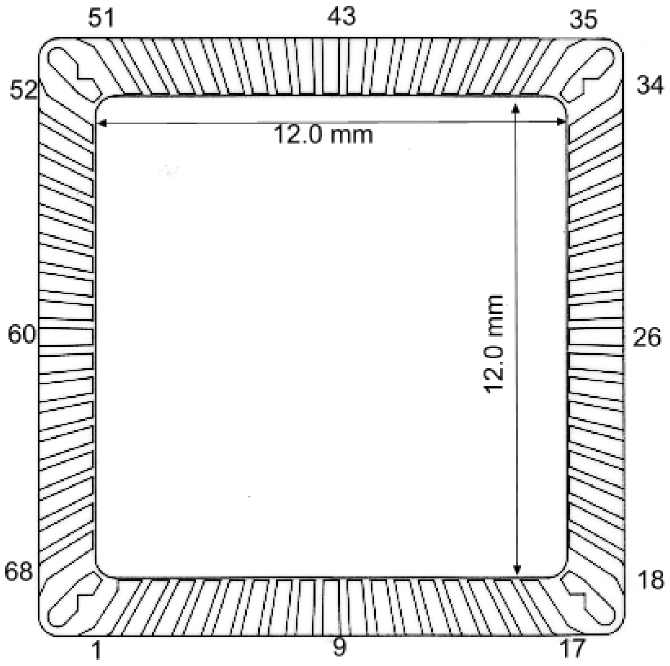

Figure 5.2 (a): Top View of aPGA-68 package.

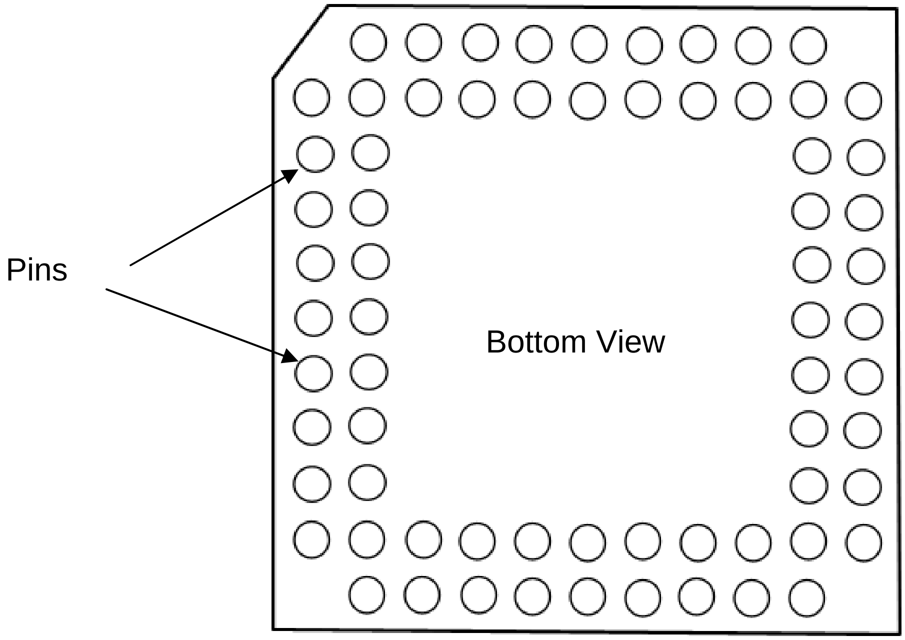

Figure 5.2 (b). Bottom view of a PGA-68 package.

Table 5.1: Wire Bonding Diagram Details

Pin	Die#	Pin	Die#	Pin	Die#	Pin	Die#	Pin	Die#	Pin	Die#
1	A1	9	B1	27	A5	57	B5	59	A3	5	O
3	A2	19	B2	31	A6	55	B6	41	A5	29	O
7	A3	25	B3	33	A7	43	B7	21	B4	39	O
63	A4	11	B4	37	A8	53	B8	45	B6	61	O

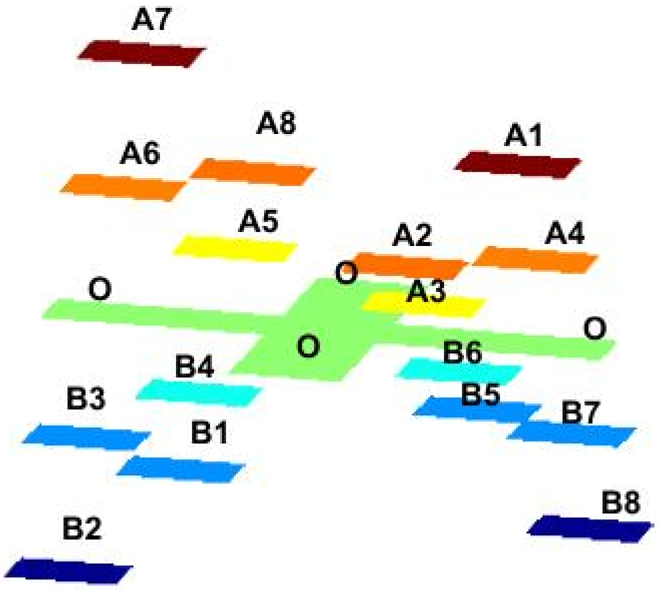

3D View for Packaging Plan

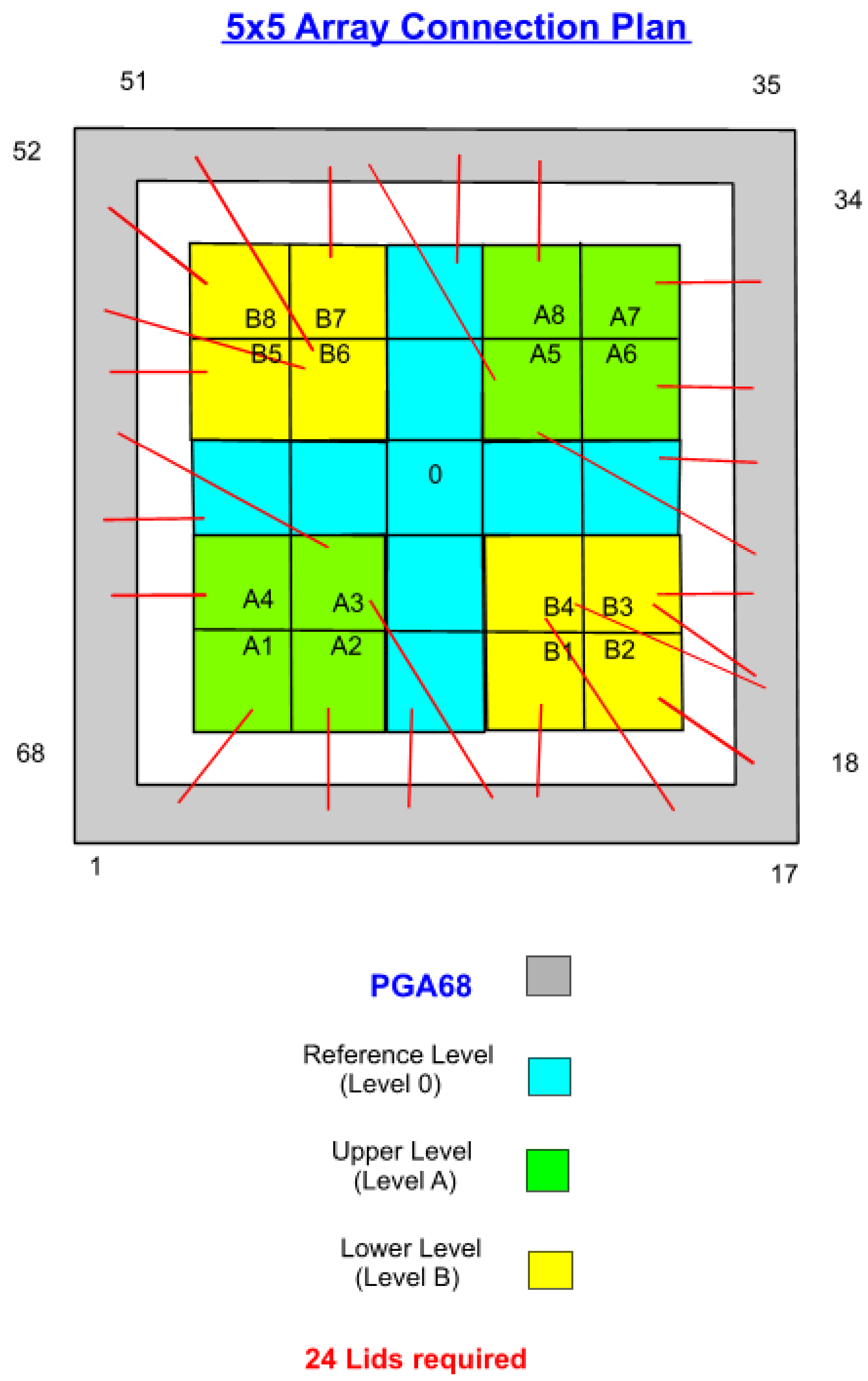

Figure 5.3. 5x5 array pin connection scheme (PGA-68 Package).

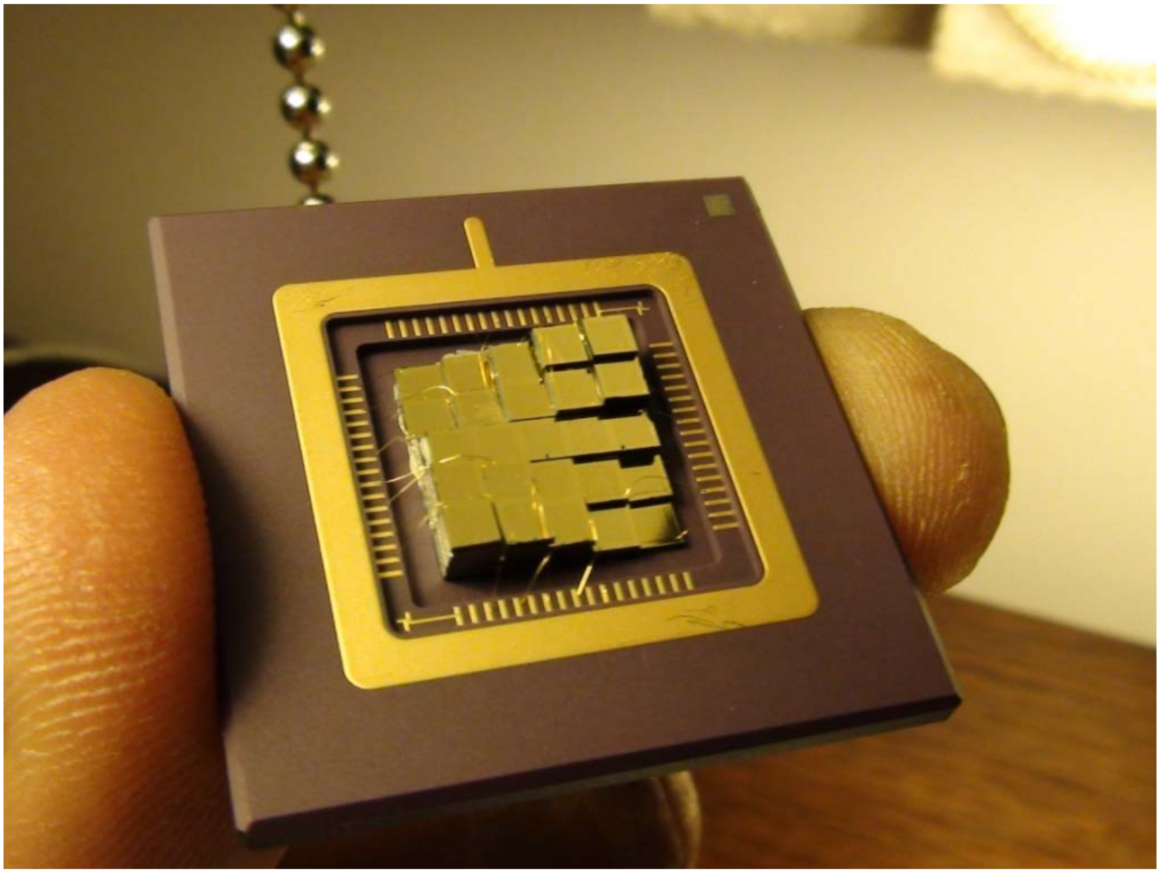

Figure 5.4: Complete 5x5 array (Top View).

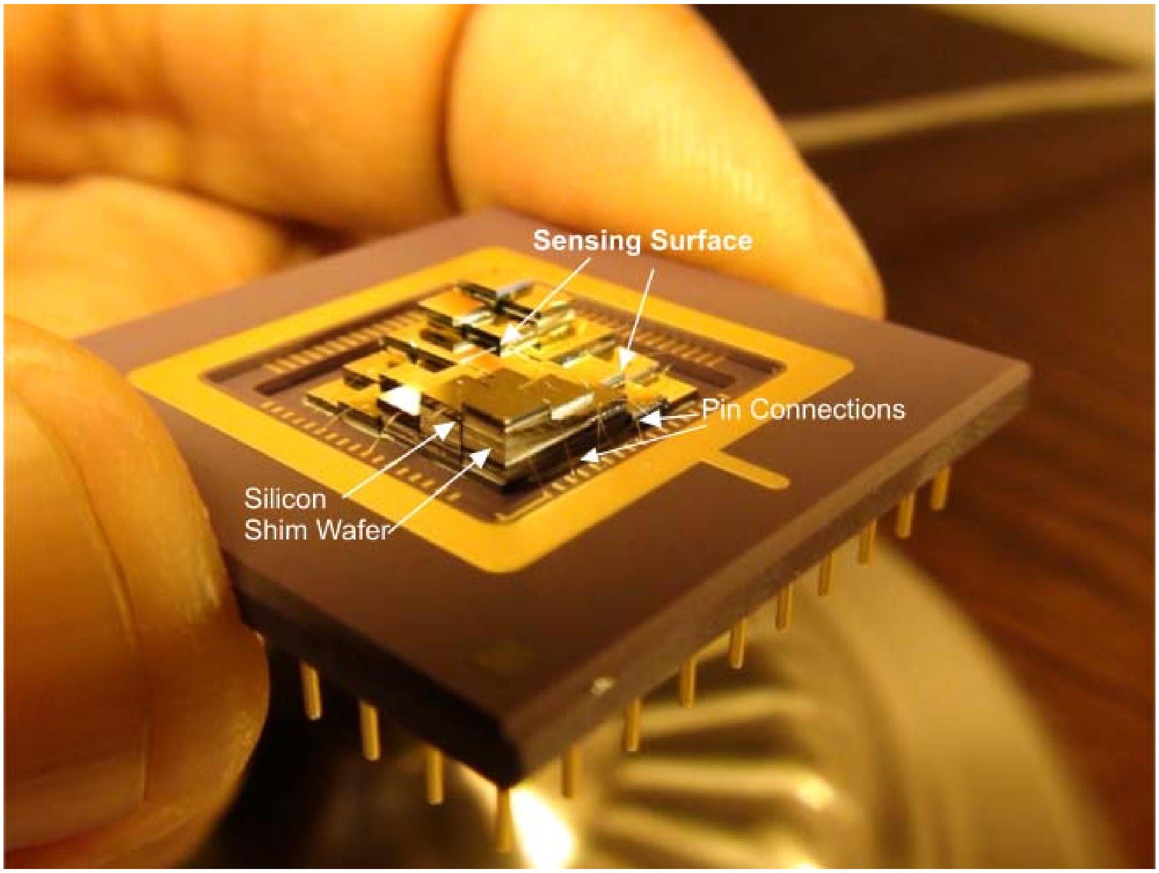

Figure 5.5: Complete 5x5 array (Side View).

Chapter 6

Conclusions and Future Work

6.1 Conclusion

A successful design, simulation, and fabrication of a non-planar Capacitive Micromachined Ultrasonic Transducer (CMUT) array that can provide a frequency independent constant bandwidth broadband beamforming capability without any microelectronic signal processing has been carried out in this thesis.

Current beamforming solutions involve microelectronics based complex algorithms, making these systems more complex and subject to processing time latency. A discrete hyperbolic paraboloid shaped array which has intrinsic beamforming capabilities and hence forth can provide a cheaper and less complex solution for real time applications as compared to the currently available solutions. The array has been designed for blind spot monitoring in a future automotive collision avoidance system. The scientific approach of this research work is based on the previous work [4].

Two different designs, A 7x7 array and B 5x5 array, operating in the frequency range of 113-167 kHz, beamwidth of 20 ± 5^0, and a maximum sidelobe intensity of -6dB as suited for the target application has been carried out. The array level and transducer level geometric specifications were calculated for both. Due to the less complex assembly and packaging involved in case of 5x5 array, it was pursued for fabrication.

After simulation of the fabrication process using IntelliFab module of IntelliSuite™, the actual fabrication of the array was carried out at CIRFE, University of Waterloo. The latest Silicon-On-Insulator (SOI) based fabrication technology was used. Step by Step details of the fabrication process including the materials used, process parameters and fabrication constraints have been described in this work. The assembly and packaging details for the device have also been developed and provided along with the necessary pin connection schemes. A commercially available Pin Grid Array (PGA)-68 package has been used as it provides the required die space cavity along with the sufficient number of pins for connection. Advotech Inc. of Tempe, Arizona, USA followed the developed assembly and interconnection scheme to package the non-planar array.

A new analytical model to calculate the deflection profile of a square diaphragm capacitive sensor subject to both electrostatic and external mechanical pressure has been developed and verified by comparing the results with 3-D electromechanical finite element analysis with excellent accuracy. Another analytical model has also been developed to calculate the capacitance change of a square diaphragm capacitive type sensor subject to both external mechanical and electrostatic pressure. The model incorporates the effect of fringing field capacitance, bias voltage and spring hardening effects associated with large deflections of a diaphragm. The model exhibits excellent accuracy when compared with IntelliSuite™ finite element analysis (FEA) results.

Lumped element modeling of the capacitive transducers has been carried out to reduce the geometric complexity to a manageable level for rapid simulation and specification determination. The lumped element modelling is able to optimize the performance of the individual transducers. The design and performance parameters obtained were verified with IntelliSuite™ FEA results.

6.2 Future Work

One of the main concerns in MEMS technology is packaging. Although, a commercially available package (PGA-68) has been used in this case but an acoustical cover over the package is desired. This cover will be able to improve the ruggedness of the device and make it less prone to ambient tampering, contamination but the performance requirements for such a cover make it a research challenge.

Also the same concept of intrinsic beamforming can be extended for medical diagnostic applications as well. In case of brain scanning, where a frequency in MHz range is used, we can have several such small arrays encircling the area of investigation and hence an image can be generated for further analysis. For a frequency range of 0.8-1.4 MHz, an array design has been presented here in table 6.1. Further investigation in this area can help to provide cheaper solutions in the field of medical diagnostic imaging as well.

Table 6.1: Brain Scan Array Specifications

Parameter	**For 21x21 Array**	**Unit**
Operating Frequency Range	0.8—1.4	MHz
Beamwidth	20° ± 4°	degrees
Array Sidelength	2.55	mm
Array Height	0.84	mm
Sensing Surfaces per axis	21	-
Elevations	22	-
Sensing Surface sidelength	120	µm
Bias Voltage	12.0	Volts

References

1. J. C. Chen, K. Yao, and R. E. Hudson, “Source localization and beamforming,” *IEEE Trans. Signal Processing*, vol. 16, no. 2, pp. 30–39, Mar. 2002.
2. B. D. V. Veen and K. M. Buckley, “Beamforming: A versatile approach to spatial filtering,” *IEEE Trans. Signal Processing*, vol. 5, no. 2, pp. 4–24, Apr. 1998.
3. D. George, J. Markwell, and R. Fogarty, “Real-time sonar beamforming on high-performance distributed computers,” *Parallel Comput*., vol. 26, no. 10, pp. 1231–1252, Sep. 2000.
4. M. Meloche and S. Chowdhury, “Design of a MEMS Discretized Hyperbolic Paraboloid Geometry Ultrasonic Sensor Microarray ,” *IEEE Trans. Ultra. Fero. And Freq. Control*., vol. 55, no. 6, pp. 1363–1372, June 2008.
5. T.C Chou, “Broadband Frequency Independent Beamforming,” Master’s thesis, MIT, 1995.
6. M. Meloche, “A MEMS Non-Planar Ultrasonic Microarray,” Master’s thesis, University of Windsor, 2007.
7. I. Oppenheim, A. Jain, and D. Greve, “MEMS Ultrasonic Transducer for Testing of Solids,” *Journal of Ultr. Fer. And Freq. Contr.* 2006, vol. 50, no.3, pp. 305-311, March 2003.
8. D. T. Yeh, et.al., “3D Ultrasound Imaging using a Forward Looking CMUT Ring Array for Intravascular/Intracardiac Applications ,” *Journal of Ultr. Fer. And Freq. Contr.*, vol. 53, no.6, pp. 1202-1212, 2006.
9. M. J. Anderson, et.al., “Broadband Electrostatic Transducer: Modeling and Experimensts,” *Journal of Acoustical Soc. Of Amer.*, vol. 97, no.1, pp. 262-272, 1995.
10. J. Morris, “Broad-band constant beam-width transducers,” *J.Sound Vibr*., vol. 1, pp. 28–40, 1964.

11. J. Stewart, *Calculus: Early Transcendentals*. 5th ed. New York: Brooks Cole, 2002.
12. “Automotive Collision Avoidance System Field Operational Test,” National Highway Traffic Safety Administration (NHTSA), Tech. Rep. DOT HS 809 600, May 2003.
13. R. Seip, B. Adamczyk, and D. Rundell, “Use of Ultrasound in Automotive Interior Occupancy Sensing: Optimum frequency, Beamwidth, and SNR from Empirical Data”, *IEEE Ultrasonic Symposium*, pp. 749-751, 1999.
14. D. T. Yeh et.al., “3D Ultrasound Imaging using a Forward Looking CMUT Ring Array for Intravascular/Intracardiac Applications ,” *Journal of Ultr. Fer. And Freq. Contr.* vol. 53, no.6, pp. 1202-1212, 2006.
15. P.C. Hzu, et.al., “A High Sensitivity Polysilicon Diaphragm Condenser Microphone,” *Eleventh Annual International Workshop on MEMS,* Germany*,* 1998.
16. Y. Huang, et.al., “Fabricating CMUT with Wafer-bonding Technology,” *Journal of MEMS.*, vol. 12, no.2, pp. 128-137, 2003.
17. T. B. Gabrielson, “Mechanical-Thermal Noise in Micromachined Acoustic and Vibration Sensors,” *IEEE Trans. On Electron Devices*, vol. 40, mo.5, pp. 903-909, May 1993.
18. I. Laudabaum, “Surface Micromachined Capacitive Ultrasonic Transducers,” *Journal of Ultr. Fer. And Freq. Contr.*, vol. 45, no. 3, pp. 679-690, 1999.
19. S. D. Senturia, *Microsystem Design*. Kluwer Academic Publishers, 2001.
20. I. J. Oppenheim, A. Jian, and D. W. Greve, “Electrical Characterisation of Coupled and Uncoupled MEMS Ultrasonic Transducers,” *Journal of Ultr. Fer. And Freq. Contr.,* vol. 50, no.3, pp. 297-304, March 2003.
21. P.-C. Hzu, C. Mastrangelo, and K. Wise, “ A high Sensitivity Polysilicon Diaphragm Condenser Microphone,” *The Eleventh Annual International Workshop on MEMS, 1998,* Heidelburg, Germany, 1998, pp. 591-596.

22. S. Chowdhury, “ Microelectromechanical (MEMS) VLSI Structures for Hearing Instruments,” Master’s Thesis, University of Windsor, Canada, 2000.
23. R. Puers and D. Lapadatu, “Electrostatic Forces and their Effects on Capacitive Mechanical Sensors,” *Physical Sensors and Actuators A,* vol. 56, no. 3, pp.203-210, 1996.
24. S. Chowdhury, M. Ahmadi, and W. Miller, “A New Analytical Model for the Pull-in Voltage of Clamped Diaphragms Subject to Electrostatic Force,” *Sensor Letters*, vol. 2, no. 2. pp. 106-112, June 2004.
25. S. Natrajan and A. Marshall, “Technological Innovations to Advance Scalability and Interconnects in Bulk and SOI”, *Proceedings of the 15th International Conference on VLSI Design (VLSID.02),*2002
26. “Annual Report,” http://www.soiconsortium.org/about-soi/economics-benefits.php, SOI Industry Consortium, official website, March 2009.
27. T. B. Oogarah, “Training Guide for New Clean room users”, Processes and Procedures, *CIRFE,* University of Waterloo, Feb’2008.
28. T. B. Oogarah, “Photolithography”, Processes and Procedures, *CIRFE,* University of Waterloo, May’2007.
29. “UW-MEMS Design Handbook,” *CIRFE*, University of Waterloo, Document Version 2.0.
30. K. R. Williams, K Gupta, and M. Wasilik, “Etch Rates for Micromachining Processing- Part-II,” *Journal of Microelectromechanical Systems*, vol. 12, no. 6, pp. 761-778, December’ 2003.
31. “Operating Manual,” Automegasamdri-915B, Series C Critical Point CO2 Dryer.
32. R. D. Gerke, “MEMS Packaging,” Chapter 8, Available online http://parts.jpl.nasa.gov/docs/JPL%20PUB%2099-1H.pdf.
33. Bergqvist, J. and Gobet, J., “Capacitive microphone with a surface micromachined backplate using electroplating technology”, *Journal of Microelectromechanical Systems*, vol. 3, pp. 69-74, 1994.

34. Eaton, W.P. and Smith, J.H., “Micromachined pressure sensors: review and recent developments”, Journal of Smart Material Structures, Vol. 6, pp. 530-9., 1997.
35. N. V. D. Meijs, and J. T. Fokkema, “VLSI Circuit Reconstruction from Mask Topology”, Integration, Vol. 2, No. 2, pp. 85-119, March 1984.
36. H. E. Elgamel, “A Simple and Efficient Technique for the Simulation of Capacitive Pressure Transducers”, *Sensors and Actuators A*, vol. 77, pp. 183–186, Nov. 1999.
37. S. Timoshenko and S. Woinowsky-Krieger, *Theory of Plates and Shells*, McGraw-Hill, New York, 2nd edn., pp.396-424, 1959.
38. D. Maier-Schneider, J. Maibach, and E. Obermeier, “A New Analytical Solution for the Load-Deflection of Square Membranes”, J*. of Microelectromechanical Systems*, vol. 4, pp. 238-241, 1995.
39. H. E. Elgamel, “Closed-Form Expression of the Relationships Between Stress, Membrane Deflection, and Resistance Change with Pressure in Silicon Piezoresistive Pressure Sensors”, *Sensors and Actuators A*, vol. 50, pp. 17–22, 1995.
40. S. Chowdhury, “A MEMS Acoustical Sensor Array and Associated Micropackage,” Ph.D. dissertation, University of Windsor, Canada, 2003.
41. K. A. Wong, S. Panda, and I. Laudabaum, “Curved Micromachined Ultrasoic Transducers,” in 2003 *IEEE Symp. On Ultrasonic, Ferroelectrics and Frequency Control,* vol. 1, October 2003, pp.572-576.
42. D. G. Tucker, “Arrays with constant beam-width over a wide frequency-range,” *Nature*, vol. 180, no. 496, pp. 497–498, Sep. 1957.

Appendix A

Matlab Scripts

A.1 Center Deflection Vs Biasing Voltage

```
% Center Deflection evaluation Using the proposed analytical method. (Chapter Three)
% Coded by:-  Syed Yasir Abbas
% Date: - 26th June 2008
% Modified: -  24th April 2009.
clear all;
close all;
L=225e-6; % Sidelength in micrometer
a=L/2;      % Half of side length
t=2e-6;     %Thickness of diaphragm
v=0.35;      % Poisson’s Ratio
E=160e9/(1-v^2); % Effective Young's Modulus in Pa
A=L^2;
Cs=1.994;
Fs=(1-0.271*v)/(1-v);
Cb=4.06;
Cr=3.45;
D=E*t^3/(12*(1-v^2));
eps0=8.853e-12;
CD=[ ];
for m=0:6;
sigma(m+1)=(30e6); %Residual Stress in Pa
P(m+1) = 000 ;  % Applied Pressure in Pascal
V(m+1)=10*m; % Bias Voltage Volts
d(m+1)= (1e-6); %Air Gap
% Solving the cubic equation for the Center Deflection (Combined Model).
```

```
A3= Cs*Fs*(E*t/a^4);
A2=0;
A1=(Cr*sigma(m+1)*t/a^2)+(Cb*12*D/a^4)-
(eps0*V(m+1)^2/(2*a))*((2*a/d(m+1)^3)+(0.33125*a^0.25/d(m+1)^2.25));
A0= -(P(m+1)+(eps0*V(m+1)^2/(2*a))*((a/d(m+1)^2)+(0.265*a^0.25/d(m+1)^1.25)));
W =roots ([A3 A2 A1 A0]);
for n=1:length(W)
   if ((imag(W(n))== 0))
            Wo =W(n);
   end
end
CD(m+1)= Wo/(1e-6); % Center Deflection in micrometer
C(m+1) = dblquad(@cap,-L/2,L/2,-L/2,L/2,[],[],Wo);
end
Plot (V,CD,'b');
Xlabel ('Biasing Voltage(Volts)');
Ylabel ('Center Deflection (Micrometer)');
```

A.2 Capacitance Vs Biasing Voltage

```
% Center Deflection evaluation Using the proposed analytical method. (Chapter Three)
% Coded by:-  Syed Yasir Abbas
% Date: - 26th June 2008
% Modified: -  25th April 2009.
clear all;
close all;
L=225e-6; % Sidelength in micrometer
a=L/2;      % Half of side length
t=2e-6;     %Thickness of diaphragm
v=0.35;     % Poisson’s Ratio
E=160e9/(1-v^2); % Effective Young's Modulus in Pa
A=L^2;
Cs=1.994;
Fs=(1-0.271*v)/(1-v);
Cb=4.06;
Cr=3.45;
D=E*t^3/(12*(1-v^2));
eps0=8.853e-12;
CD=[ ];
for m=0:6;
sigma(m+1)=(30e6); %Residual Stress in Pa
P(m+1) = 000 ;  % Applied Pressure in Pascal
V(m+1)=10*m; % Bias Voltage Volts
d(m+1)= (1e-6); %Air Gap
% Solving the cubic equation for the Center Deflection (Combined Model).
```

```
A3= Cs*Fs*(E*t/a^4);
A2=0;
A1=(Cr*sigma(m+1)*t/a^2)+(Cb*12*D/a^4)-
(eps0*V(m+1)^2/(2*a))*((2*a/d(m+1)^3)+(0.33125*a^0.25/d(m+1)^2.25));
A0= -(P(m+1)+(eps0*V(m+1)^2/(2*a))*((a/d(m+1)^2)+(0.265*a^0.25/d(m+1)^1.25)));
W =roots ([A3 A2 A1 A0]);
for n=1:length(W)
   if ((imag(W(n))== 0))
            Wo =W(n);
   end
end
CD(m+1)= Wo/(1e-6); % Center Deflection in micrometer
C(m+1) = dblquad(@cap,-L/2,L/2,-L/2,L/2,[],[],Wo);
end
C=C/10^-12;  %Capacitance pF
Plot (V,C,'b');
Xlabel ('Biasing Voltage(Volts)');
Ylabel (`Capacitance (pF)');
```

A.3 Lumped Element Simulation

```
% Array Design Simulation.
% Coded by:- S Yasir Abbas
% Dated:- 29th Feb'2008.
clear all;
clc;
physical.Vb= 18;              % Biased Voltage (Volts), according to car battery O/P.
physical.eta = 17.1*10^-6; % Air Viscocity.
physical.rhoO= 1.21;         % Air Density.
physical.E = 1.6*10^11;   % Young's Modulus.
physical.Rs =30*10^6;     % Residual Stress.
physical.v = 0.35;            % Poisson's ratio.
physical.epsO =8.85*10^-12; % Electrical Permittivity.
physical.omega = 2*pi*(140e3); % Operating frequency in rads/sec.
physical.P = 1;           % Acoustic Pressure.
physical.Temp = 90;       % System Temperature in Celsius.
physical.c= 343;          % Speed of Sound in Air.
physical.a=.225e-3;       % Diaphragm Side length in meter.
physical.d= 1*10^(-6);    % Air Gap in meter.
physical.t= 2*10^(-6);    % Diaphragm Thickness.
physical.rho= 2300;       % Density of Diaphragm material.
physical.holes = 5*5;     % Nos. of holes in perforated plate.
physical.elements  = 6*6; % Elements per Tier
physical.rbh = 15e-6;
physical.omegaLower=2*pi*(113e3);
physical.omegaUpper=2*pi*(167e3);
```

```
% Determine Lump model parameters from physical parameters and physical
% properties. Model given by [21,23] is used.
lump = genlumped(physical);
% Resonant Freq and Steady State response
%Determine mechanical steady state response with respect to frequency as
%well as undamped resonant frequency.
[freq,Resp,Fres,Sop]=freqresponse(physical,lump);
%Determine the electrical sensitivity as per Mastrnagelo paper
Smast = abs(mastrangelo(physical))*10^3;  %Express in mV/Pa
% Determine capacitance of tier based on parallel plate approximation.
Cdia = (physical.epsO*physical.a^2/physical.d)*physical.elements;
%Percentage area of Diaphragm area occupied by  vents.
alpha=lump.alpha*100;
% Determine Mechanical sensitivity and capacitance change by puers method
Spuers=puers(physical);

% generate report
disp( date );
disp ('_____Transducer Parameters______________________');
disp(['Diaphragm side length:' num2str(physical.a*10^3) ' mm']);
disp (['Diaphragm thickness: ' num2str(physical.t*10^6) ' micrometer']);
disp (['Air Gap /Buried Oxide thickness: ' num2str(physical.d*10^6) ' micrometer']);
disp('-----------Lumped Element Model Results-------    ' );
disp(['Unbiased Tier Capacitance: ' num2str(Cdia*10^12) 'pF']);
disp(['Resonant frequency: ' num2str(Fres/10^3) 'kHz']);
        disp('****************************');
disp('**********Sensitivity figures*********' );
```

```
disp(['Mechanical Sensitivity by puers method: ' num2str(Spuers.Sz*10^6) 'um/N @'
num2str(physical.omega/(2*pi*10^3)) 'kHz' ]);
disp('**********************************');
disp(['Capacitance change (per Tier) by puers method:   '
num2str(Spuers.deltaC_AC*10^15*physical.elements) 'fF/Pa @'
num2str(physical.omega/(2*pi*10^3)) 'kHz' ]);
disp('**********************************');
disp(['Diaphragm Total Sensitivity by Resonance Method: ' num2str(Sop*10^3) '
(mV/Pa)/element @' num2str(physical.omega/(2*pi*10^3)) 'kHz' ]);
disp(['Diaphragm Total Sensitivity by Mastrangelo Method: ' num2str(Smast) '
(mV/Pa)/element @' num2str(physical.omega/(2*pi*10^3)) 'kHz' ]);
disp(['Total Tier sensitivity predicted between : ' num2str(physical.elements*Smast) '--'
num2str(physical.elements*Sop*10^3)  '(mV/Pa) @'
num2str(physical.omega/(2*pi*10^3)) 'kHz' ]);
disp('---------');
disp (['Percentage of diaphragm area occupied by vent holes: ' num2str(lump.alpha*100)
'%']);
```

A.4 Beam Shape Codes

```
% Codes Provide polar plot of power in terms of theta and give
% a picture of mainlobe and sidelobe power.
% Coded by: Syed Yasir Abbas
% Last updated on 9th Feb'2008.
close all;
ML=2; %sidelength in terms of wavelength along X-axis (=3,113;=2.42,140;=2,167).
MY=2; %sidelength in terms of wavelength along Y-axis.
alpha =10*pi/180;
M=5; %Nos of sensors per axis
theta =(-90:2:90)*pi/180;
phi = (0:1:0)*pi/180;
pMain = zeros(length(ML),1);
pSide= 0;
for index= 1:length(ML)
   L=ML(index);
   Y=MY(index);
   Z= zeros(length(theta),length(phi));
   for a=1:length(theta)
      for b= 1:length(phi)
         Z(a,b)=DiscSens(theta(a),phi(b),L,Y,alpha,M);
      end
   end
% Normalize Z
Z=Z/max(max(Z));
% Total Power from -pi/2 to pi/2.
```

```
ledge=nmatch(theta,-pi/2);
redge=nmatch(theta,pi/2);
ptheta=theta(ledge:redge);
pZ=Z(ledge:redge);
pTotal(index)=trapz(ptheta,abs(pZ));
%Power in Main Lobe from -alpha to alpha.
ledge=nmatch(theta,-alpha);
redge=nmatch(theta,alpha);
ptheta=theta(ledge:redge);
pZ=Z(ledge:redge);
pMain(index)= trapz(ptheta, abs(pZ));
% Power in Sidelobe
pSide(index)=1-abs(pMain(index))/abs(pTotal(index));
end
num2str(L),'Lambda']);
figure,
mmpolar(theta,abs(Z));
mmpolar('TTickValue',[350,10,90,270,45,315,170,190,135,225]);
mmpolar('RTickValue',[0.5012,0.3162,0.8913]);
mmpolar('RTickLabel',{'-6dB', '-10dB', '-1dB'});
mmpolar('RTickLabelValign','cap');
```

A.5 Code for Generating Discrete Hyperbolic Paraboloid

```
% Discrete Hyperbolic Paraboloid plot for 5x5 array.
% Coded by:- SYED YASIR ABBAS.
% LAST UPDATED:-21st DEC'2007 .
x=-2:2;
y=-2:2;y=y';
z=y*tan(20*x/6);
k=zeros(length(x),length(y));
[X,Y]=meshgrid(x,y);
grid off;
hold on;
y=-2;
for m = 1:length(X); %:length(x)
   x=-2;
for n = 1:length(Y); %:length(y)
h=ones(length(X),length(Y));
   h=z(m,n)*h;              %h,length(h),
s= x-0.5:(0.5/2):x+0.5;
w= y-0.5:(0.5/2):y+0.5;
[X,Y]=meshgrid(s,w);       %length(X),
surf(X,Y,h)%,'fill','r');
shading flat;
x=x+1;
end
y=y+1;
end
```

Vita Auctoris

Syed Yasir Abbas (Rizvi) was born in 1984 in Barabanki, India. He completed his Bachelors in Electrical Engineering (B.Tech) from Z.H.C.E.T, Aligarh Muslim University (India), in 2006. He received International Graduate Student Scholarship at University of Windsor and also Siemens Budding Technocrat Scholarship in India.